Materials & Design 254 (2025) 114072

Contents lists available at ScienceDirect

Materials & Design

journal homepage: www.elsevier.com/locate/matdes

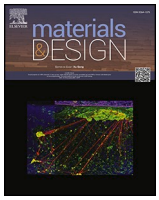

# Contrasting effects of Si on high-temperature deformation behavior and room-temperature strength in V-microalloyed 10Mn-18Cr stainless steels

Atef Hamada [a,*], Ali Khosravifard [b], Khaled Elanany [c], Mahmoud Khedr [a,d], Anna Kisko [e], Matias Jaskari [a], Saad Ebied [f], Tarek Allam [g,1], Antti Järvenpää [a], Pentti Karjalainen [h]

[a] Kerttu Saalasti Institute, Future Manufacturing Technologies (FMT), University of Oulu, Pajatie 5, FI-85500 Nivala, Finland
[b] Department of Materials and Metallurgical Engineering, Abadeh Higher Education Center, Shiraz University, Abadeh 73916, Iran
[c] Department of Ferrous Metallurgy, Montanuniversität Leoben, Franz-Josef-Straße 18, 8700 Leoben, Austria
[d] Mechanical Engineering Department, Faculty of Engineering at Shoubra, Benha University, Cairo 11629, Egypt
[e] Hydro Aluminium AS, Hydro Aluminium Sunndal, R&D, Romsdalsvegen 1, NO-6601 Sunndalsøra Norway
[f] Department of Production Engineering and Mechanical Design, Faculty of Engineering, Tanta University, Tanta 31527, Egypt
[g] Institute of Energy Materials and Devices - Structure and Function of Materials (IMD−1), Forschungszentrum Jülich GmbH, 52428 Jülich, Germany
[h] Materials and Mechanical Engineering, Centre for Advanced Steels Research, University of Oulu FI-90014 Oulu, Finland

ARTICLE INFO

*Keywords:*
MnCr stainless steel
Si alloying
High-temperature deformation
Mechanical properties
Ferrite phase
Microstructure

ABSTRACT

Two MnCr stainless steels (0.17C-10Mn-18Cr-xSi-1V-0.25N, wt.%) with varying Si contents (x=0.4 and 2.2 wt. %) were designed with a stacking fault energy of 35 mJ/m$^2$ to activate the TWIP effect. The high-temperature deformation behavior and room-temperature (RT) tensile properties were investigated to explore the impact of Si in both high and RT regimes. The high-temperature behavior of the steels was assessed using hot-rolled plates through compression tests at temperatures ranging from 950 to 1100 °C and strain rates from 0.01 to 10 s$^{-1}$. Hot deformation processing maps were established to identify the safe and unstable deformation zones. The RT tensile properties were evaluated through uniaxial tensile tests of fast-heating (FH) annealed cold-rolled sheets at temperatures ranging from 800 to 1200 °C for 3 min. Microstructural analysis of the hot-rolled and FH annealed structures was conducted using electron backscatter diffraction and laser scanning confocal microscopy, and precipitation was characterized by transmission electron microscopy. The findings demonstrated that MnCr-V steel with higher Si content (2.2 wt.%) had reduced hot-deformation resistance and lower activation energy for deformation (477 kJ/mol) compared to its lower Si counterpart (507 kJ/mol). This can be attributed to the soft ferrite phase within the austenite during elevated temperature tests. Conversely, the RT tensile properties exhibited an opposite trend, with the high Si steel showing increased yield strength (YS) and Ultimate tensile strength (UTS) compared to the low Si steel. This improvement is due to solid solution strengthening from Si, precipitation strengthening from V(C,N) particles, and a fine-grained recrystallized structure resulting from short annealing. For instance, after a FH process at 1000 °C for 3 min, the YS, UTS, and total elongation values were 665 MPa, 980 MPa, and 40 %, respectively, for the low Si steel, while the high Si steel achieved values of 715 MPa, 1045 MPa, and 30 %, respectively. Mechanical twinning was evident in both materials.

## 1. Introduction

Austenitic steels containing Mn, especially those demonstrating twinning-induced plasticity (TWIP) and transformation-induced plasticity (TRIP), are increasingly recognized as strong contenders for structural applications that demand a suitable combination of high strength and ductility [1,2]. TWIP steels containing 12–35 wt.% Mn are notable for their capacity to experience substantial mechanical twinning during plastic deformation. This property dramatically improves their strain-hardening ability and contributes to high ductility, even at elevated temperatures [1–4]. However, challenges involving production and high material costs limit their applications. Medium-Mn steels, defined by Mn levels ranging from 3 to 12 wt.%, exhibit a ferritic/martensitic-austenitic structure microstructure, [5]. Recently, there

* Corresponding author.
*E-mail address:* atef.hamadasaleh@oulu.fi (A. Hamada).
[1] On an unpaid leave from Department of Metallurgical and Materials Engineering, Suez University, 43528, Suez, Egypt.

https://doi.org/10.1016/j.matdes.2025.114072
Received 5 February 2025; Received in revised form 29 April 2025; Accepted 6 May 2025
Available online 10 May 2025

has been significant interest, with ultimate tensile strength (UTS) exceeding 1.5 GPa and total elongation (TE) greater than 15 %, particularly due to the TWIP effect [1]. Nonetheless, the corrosion and hydrogen embrittlement resistances of these steels are inadequate, leading to the development of austenitic medium-Mn steels with high Cr content [6]. Commercial MnCr AISI 2XX grade steels have been widely used since the 1950 s in various applications. In these steels, Mn (approximately 5–8 %) and N act as cost-effective austenite-promoting elements that replace Ni. Furthermore, the TWIP effect positively enhances the combination of strength and ductility properties [7]. Nevertheless, achieving an optimal balance between strength and ductility in medium-Mn TWIP steels, especially during high-temperature deformation, is still a significant challenge in materials design and innovation [8,9]. Outokumpu Oy in Finland has developed a new grade of fully austenitic MnCr stainless steel called Forta H, specifically designed for use in safety–critical structural components of vehicles [10].

The TWIP effect is fundamentally associated with stacking fault energy (SFE), as twinning occurs when SFE is between 18 and 45 $mJ{\cdot}m^{-2}$ [11,12]. On one hand, SFE is influenced not just by chemical composition but also by temperature. Consequently, at higher temperatures, SFE increases, encouraging dislocation glide over mechanical twinning, negatively impacting the work-hardening rate [13,14]. Conversely, SFE relies on the contents of Mn and Cr, in addition to alloying elements like C, Al, and Si [15,16]. By modifying Si levels to decrease the SFE, we can tailor the SFE and, consequently, the microstructure, enhancing the mechanical performance of medium-Mn TWIP steels at both room temperature (RT) and elevated temperatures [16,17].

Recent studies have highlighted the role of Si in enhancing the mechanical properties of high-Mn TWIP steels by influencing the phase stability, deformation mechanisms, and microstructural evolution during thermomechanical processing and hot ductility [18,19]. Si is recognized as a ferrite stabilizer that promotes ferrite formation, softening the material during hot deformation. However, it also acts as a powerful solid solution strengthening element, enhancing yield strength (YS) at RT [20]. However, the effects of varying Si content on high-temperature deformation behavior and subsequent RT mechanical strength, particularly in V-microalloyed TWIP-type MnCr stainless steels, are scarcely reported in the literature.

Microalloying with V adds complexity to the microstructural evolution of TWIP steels, primarily through precipitation strengthening due to the formation of V(C,N) [21]. VC particles significantly enhance the strength of TWIP steels at cryogenic temperatures, particularly in recrystallized or refined grain structures [22]. Furthermore, these particles hinder the TRIP effect in medium-Mn steel [23]. Nonetheless, the interplay of Si and V and their joint impact on high-temperature deformation behavior and RT mechanical properties is still an unresolved issue that mandates thorough examination.

The high-temperature deformation of TWIP steels, particularly during thermomechanical processing, is crucial for controlling the grain size, recrystallisation behavior, and texture evolution [24]. The flow characteristics of TWIP steels at high temperatures significantly rely on factors such as alloying elements, temperature, strain rate, and the initiation of dynamic recrystallization (DRX) [25]. DRX enhances ductility and facilitates grain refinement in austenitic stainless steels [26]. Adding Si can improve DRX by lowering the SFE and encouraging twinning, affecting recrystallization kinetics during hot deformation [27]. Moreover, Si is known to enhance the work-hardening characteristics of high-Mn TWIP steels through solid solution strengthening and improved twinning, which leads to increased yield and tensile strengths [18].

In terms of high-temperature deformation, the plastic behaviour of TWIP steels is typically analysed through hot-compression tests, which provide insights into the flow stress level and its temperature dependence, i.e., the activation energy of deformation, as well as the strain rate sensitivity [28,29]. Flow stress data, often interpreted using the Zener–Hollomon parameter, are critical for understanding the hot workability of a material and the mechanisms governing DRX [30,31]. However, the effect of Si on the activation energy of deformation, which indicates the energy barrier for dislocation motion and DRX, needs further clarification in the context of V-microalloyed TWIP steel. The interaction between Si-induced softening and V(C,N)-induced precipitation strengthening may significantly change the deformation mechanisms, especially at high temperatures.

At RT, the mechanical behavior of TWIP steels is affected by the synergistic effects of solid solution strengthening, twinning, and precipitation hardening [32,33], enhanced by Si alloying. They result in improved YS and UTS, and the effect is particularly pronounced after cold rolling and annealing. Si accelerates recrystallization by decreasing the SFE, which supports the dislocation density needed for enhanced recrystallization [27].

The role of Si in the deformation mechanisms of TWIP and TRIP steels is relatively well understood; however, its specific contributions to V-microalloyed MnCr stainless steels have not been thoroughly explored. The dual effects of Si in promoting δ-ferrite formation and softening at elevated temperatures, while enhancing solid solution strengthening and influencing grain structure changes at RT have not been systematically studied. Additionally, the relationships between Si and microalloying elements like V, as well as its impact on recrystallization and precipitation during thermomechanical processing, remain ambiguous. This study aims to address this knowledge gap by examining how Si influences the hot deformation behavior and mechanical properties at RT across various microstructural states, thereby offering clearer insight into its dual functionality within this advanced alloy system.

This study examines the dual function of Si in a V-microalloyed medium-Mn steel that contains chromium, vanadium, and some nitrogen. It focuses on high-temperature deformation behavior and RT mechanical strength. While previous research has looked at the general influence of Si in TWIP steels, this study is distinct in combining hot compression testing at elevated temperatures with tensile testing of cold-rolled and briefly annealed steels. This approach reveals how different Si levels affect recrystallization, grain size, and strength development over a wide range of annealing temperatures (800–1200 °C). The integration of advanced microstructural characterization techniques, such as electron backscatter diffraction (EBSD) and a laser scanning confocal microscope (LSCM), allows for an in-depth analysis of the role of Si in strengthening mechanisms and deformation behavior. Furthermore, this study offers new insights into the interaction between Si content, V microalloying, and V(C,N) precipitates, highlighting critical pathways for optimizing both formability and strength in medium-Mn TWIP-type steels while providing a valuable foundation for the design of high-performance steels for applications across a wide range of temperatures.

Several critical aspects regarding the combined effects of alloy composition, SFE, and phase stability under thermomechanical conditions remain inadequately addressed. Even with extensive studies on high-Mn steels and 200-series stainless steels, the impact of Si on the interplay of SFE, phase stability, and deformation mechanisms in V-microalloyed Mn-Cr stainless steels is still not well understood. While it is established that Si can influence SFE and stabilize ferritic phases at high temperatures, its dual effect, promoting δ-ferrite formation during thermomechanical processing while simultaneously enhancing solid solution strengthening at room temperature, has not been systematically explored in these complex alloy systems. Furthermore, the role of V(C,N) precipitates, which are critical for precipitation strengthening, and their interaction with the Si-modified matrix under varying thermomechanical conditions are not well characterized. This study aims to fill these critical gaps by investigating the contrasting effects of Si on both high-temperature deformation behavior and room-temperature mechanical properties in V-microalloyed MnCr stainless steels. The study focuses on the effects of Si on phase stability, particularly the retention of δ-ferrite,

SFE evolution, grain structure development, and precipitation behavior during thermomechanical processing. By adopting this comprehensive approach, the research aims to unveil new perspectives on the relationship between alloy composition, phase stability, and mechanical performance, essential for enhancing the processing and use of advanced austenitic stainless steels.

## 2. Experimental procedures

### 2.1. Steels

Two V-microalloyed medium-Mn, Cr-bearing, low-Ni austenitic stainless steels with varying Si content were engineered to achieve a chemical composition aimed at an SFE of 35 mJ/m$^2$ at RT, promoting the TWIP effect. The steels were produced from the following raw materials: (1) steel scrap for Fe and C; (2) low-C master alloys of ferrochrome, ferromanganese, and ferrosilicon as primary sources of Cr, Mn, and Si, respectively; (3) pure Ni metal; and (4) Nitrovan as a source of V and N. An open induction furnace with a 50 kg capacity was utilized for melting, and the molten steel was cast into Y-shaped blocks measuring 60 mm in thickness. The chemical compositions of the steels and their corresponding codes are provided in Table 1. A homogenization treatment was conducted at 1200 °C for 4 h to minimize segregation of alloying elements in the cast structure.

This treatment achieves microstructural homogenization and minimizes the presence of coarse precipitates. This temperature, 1200 °C, was chosen according to the Carbide Dissolution Temperature from the Thermo-Calc database, indicating that the dissolution temperatures of VC and Cr-rich carbides (i.e., $Cr_{23}C_6$) in the compositions studied are below 1200 °C.

The dissolution behavior of carbides and carbonitrides in the studied steels was evaluated to justify the solution treatment conditions. The dissolution temperature of VC was estimated using the solubility product relationship [34].

$$log[V][C] = 4.237 - \frac{6157}{T} \quad (1)$$

where [V] and [C] are the V and C contents (wt.%), and $T$ is the temperature in Kelvin. For the given compositions (1 wt.% V and 0.17 wt.% C), the dissolution temperature of VC was calculated to be approximately **957 °C**. When N was considered alongside carbon (0.25 wt.% N and 0.17 wt.% C), forming mixed V(C,N) carbonitrides, the dissolution temperature increased to approximately 1062 °C, indicating enhanced thermal stability. Moreover, according to the Thermo-Calc analysis of stable phases, as noted in Figs. S2-S3, $Cr_{23}C_6$ carbides remain stable at temperatures below 1020 °C in low-Si MnCr steel and 1120 °C in high-Si MnCr steel. These findings verify that the solution annealing process chosen at 1200 °C for 4 h effectively dissolves any coarse VC, V(C,N), and $Cr_{23}C_6$ precipitates before hot rolling, thereby ensuring a uniform austenitic matrix.

The homogenized cast materials underwent hot rolling into 12 mm-thick slabs, completed over four passes of 20 % each, with a 10 second interval between passes. The rolling began at 1200 °C, and by the end, the slabs were about 1050 °C before being water-cooled to RT.

**Table 1**
Chemical compositions of the investigated MnCr-V steels with different Si contents.

| Steel code | Composition (wt.%) | | | | | | | *Ms |
|---|---|---|---|---|---|---|---|---|
| | C | Si | Mn | Cr | Ni | V | N | °C |
| MnCr-V | 0.17 | 0.42 | 10.4 | 17.7 | 4.7 | 1.0 | 0.26 | −146 |
| MnCr-Si-V | 0.17 | 2.22 | 10.8 | 18.0 | 4.8 | 0.9 | 0.25 | −164 |

* Ms: martensite start temperature.

### 2.2. High-temperature behavior

Cylindrical specimens, measuring 8 mm in diameter and 10 mm in length, were machined from strips with the length axis aligned to the rolling direction for hot-deformation compression tests. A Gleeble 3800 thermomechanical simulator (Dynamic Systems, Inc., Poestenkill, NY, USA) was used for these tests. The specimens were heated to 1200 °C at a rate of 10 °C/s and held for 120 s to mitigate machining effects and dissolve any precipitate particles. They were then cooled at 5 °C/s to the desired test temperatures of 950, 1000, 1050, and 1100 °C and held for 30 s before being compressed to a true strain of 0.6 at constant true strain rates varying from 0.01 to 10 s$^{-1}$.

### 2.3. RT mechanical properties

In the tensile tests at RT, the 12 mm thick strips underwent a 60 % hot-rolling reduction to become 5 mm thick sheets, which were subsequently cold-rolled to a final thickness of 2 mm. These cold-rolled sheets were annealed between 800 and 1200 °C for 3 min. During the annealing process, a fast heating (FH) rate of 200 °C/s was applied using a Gleeble 3800 thermomechanical simulator, which provided certain advantages, as noted in previous studies [35–39].

The quasi-static mechanical properties at RT were evaluated using uniaxial tensile tests conducted at a strain rate of $10^{-3}$ s$^{-1}$ on a Zwick Z 100 tensile machine (Zwick Roell GmbH & Co. KG, Ulm, Germany). Standard tensile test specimens were fabricated per ASTM E 646–98 specifications, featuring a gauge length of 50 mm, a width of 12.5 mm, and an overall length of 200 mm. An extensometer recorded the strain throughout the tests.

### 2.4. Microstructure characterization

Microstructures following hot rolling, hot compression, and tensile deformation were analyzed using an LSCM (Model: KEYENCE/VK-X200, KEYENCE Corporation, Osaka, Japan). For capturing intricate microstructural details, an EBSD system integrated with a Zeiss Sigma field-emission scanning electron microscope (FE-SEM) (Carl Zeiss Microscopy GmbH, Jena, Germany) operated at an accelerating voltage of 15 kV was employed. The resulting microstructural maps were further examined with HKL-CHANNEL 5 software (Oxford Instruments, UK) to extract comprehensive statistical data on the structural characteristics.

Energy-dispersive X-ray spectroscopy (EDS) was employed, in conjunction with a transmission electron microscope (TEM) (JEOL JEM 2200FS EFTEM/STEM) operating at 200 kV, to assess the chemical compositions and identify the types of precipitates formed during FH annealing.

## 3. Results and discussion

### 3.1. Stacking fault energy (SFE) calculations

The Olson-Cohen thermodynamically based model is utilized to calculate the SFE of the studied steels at various temperatures as follows [40]:

$$SFE = 2\rho_s(\Delta G_{FCC\rightarrow HCP} + E_s) + 2\sigma_s \quad (2)$$

where $\rho_s$ is the molar surface density of atoms on the fault planes of $\{111\}_{FCC}$, $\Delta G_{FCC\rightarrow HCP}$ is the Gibbs free energy change caused by the austenite-*fcc* to martensite-*hcp* transformation, $E_s$ is the strain energy generated as a result of the transformation. $\sigma_s$ is the molar surface energy at the austenite/martensite interfaces. The contribution of strain energy ($E_s$) is small and can be neglected. The Gibbs free energy change of the transformation, i.e. $\Delta G_{FCC\rightarrow HCP}$, includes changes due to different alloying elements ($\Delta G_i^{\gamma\rightarrow\varepsilon}$) and their mutual interactions ($\Omega_{ij}^{\gamma\rightarrow\varepsilon}$) as follows:

$$\Delta G_{FCC\rightarrow HCP} = x_C \Delta G^{\gamma\rightarrow\varepsilon}_{FeMnX/C} + \sum x_i \Delta G^{\gamma\rightarrow\varepsilon}_i + \sum x_i x_j \Omega^{\gamma\rightarrow\varepsilon}_{ij} \quad (3)$$

where $x_i$ are the molar fractions of various alloying elements. All the parameters used for the Eqs. (2) and (3) are extracted from Refs. [41–44] and presented in Table 2. In order to consider the influence of N interstitial on the Gibbs free energy change, the equation developed in [41] is used.

Using the data from Table 2 and applying Eqs. (2) and (3), the SFE values were calculated for various temperatures, including RT and high-temperature deformation conditions (800–1100 °C). Table 3 summarizes the calculated SFE values. The findings reveal that the SFE values at RT slightly vary between the two steels. These values align with the TWIP regime, consistent with the documented range of 15–45mJ/m$^2$, suggesting the activity of the TWIP mechanism in austenitic Fe-Mn-based alloys [45]. However, at elevated temperatures, the SFE values increase significantly, as demonstrated in Table 3, surpassing the TWIP regime. When the SFE reaches excessively high levels, the primary deformation mechanism shifts from TWIP to cross-slip.

The contributions of alloying elements to the Gibbs free energy difference ($\Delta G\gamma \rightarrow \varepsilon$), which influences the SFE, were integrated into the Olson-Cohen thermodynamically based model to calculate the SFE. Based on the parameters in Table 2, Si negatively impacts the driving force for ε-martensite formation, with its Gibbs free energy term represented as $\Delta G_{Si} = -560 - 8T$ (J/mol). This indicates that as temperature increases, the negative contribution of Si becomes more pronounced, thereby raising the overall SFE. Although Si is not the primary element influencing SFE (compared to Mn or C), its inclusion with 2.2 wt.% can slightly increase the SFE from 34.2 to 34.7 mJ/m$^2$ in MnCr-Si-V steel.

Higher SFE values reduce the propensity for mechanical twinning, particularly at elevated temperatures. However, at RT, due to the high Mn content in both steels (~10 wt.%), the overall SFE remains sufficiently low to facilitate the TWIP effect, even in the presence of Si. Thus, while Si marginally increases the SFE, its impact at RT does not inhibit twinning. Instead, the influence becomes more pronounced at elevated temperatures, contributing to a shift in the deformation mechanism from twinning to dislocation glide and dynamic recovery.

An in-depth examination of the cutting-edge comprehension of how Si influences the SFE in Fe-Mn alloys uncovers a complex relationship. Dumay et al. [42] demonstrated that the influence of Si on SFE depends on its concentration. At low levels (< 3 wt.%), Si increases the SFE, whereas at higher levels (> 4 wt.%), it begins to decrease the SFE. This non-linear behavior indicates that the impact of Si is not straightforward but varies based on the composition and lattice structure of the alloy. The estimated SFE values in Table 3 support this trend, with the steel containing 2.2 wt.% Si showing a slightly higher SFE value of 34.7mJ/m$^2$, which stays within the range favorable for the (TWIP) mechanism.

Earlier research indicated that Si lowers the SFE of Fe-Mn-based alloys, especially when paired with specific compositions. For instance, Jeong et al.[46] observed that adding 1 wt.% Si to Fe-18Mn-0.6C steel led to a significant decrease in SFE by about 4 mJ/m$^2$.

Recent computational advancements, mainly using density functional theory, have deepened our understanding of the Si effect. Choi et al. [17] presented a theoretical investigation into the SFE of Fe-Mn-Al/Si systems, showing that the impact of Si on SFE is not isolated but is influenced by other alloying elements. Notably, interstitial elements like C and N can counteract the Si effect. These interstitial atoms alter the lattice structure through expansion, directly impacting SFE. The lattice expansion caused by these elements modifies the balance of forces governing the SF formation, thereby diminishing the role of Si in lowering the SFE [17,47]. The interaction between substitutional elements (like Si) and interstitial elements (such as C and N) indicates that Si's impact on SFE varies based on the alloy's composition and temperature.

Although this analysis provides valuable insights into the influence of Si on the SFE at both room and elevated temperatures, it is important to recognize that the simultaneous presence of other alloying elements, such as Mn, Cr, Ni, and N, also affects the observed trends. Consequently, the isolated effect of Si on SFE cannot be fully disentangled in the current alloy system, making it challenging to establish a straightforward positive or negative correlation.

Previous computational and experimental studies suggest that while Si generally influences SFE, the magnitude and direction of its effect strongly depend on the overall chemical composition and temperature. To rigorously validate the independent role of Si, future work involving systematic parametric studies, where the Si content is varied while keeping other alloying elements constant, will be necessary. Such investigations will provide a more definitive and quantitative understanding of the intrinsic impact of Si on SFE evolution.

In this context, a recent comprehensive computational study by Choi et al. [17] systematically analyzed the effect of Si on SFE in Fe-Mn-Al-Si steels using first-principles calculations. Their results demonstrated that Si addition generally decreases SFE through lattice contraction and magnetic effects, while also emphasizing that the extent of this effect varies depending on the matrix composition and thermodynamic state. These findings highlight the complex interplay between Si and other alloying elements, supporting our observation that a simple correlation between Si and SFE is not straightforward without carefully controlled experimental or computational studies. Thus, while the present conclusions are consistent with theoretical predictions, further isolated investigations are needed for complete quantitative validation.

**Table 2**
Parameters used for the calculation of the SFE of the steels based on the Olson-Cohen model.

| parameter | Expression/value |
|---|---|
| $\Delta G^{\gamma\rightarrow\varepsilon}_{Fe}$ | $-2243.38 + 4.309$ T (J/mol) |
| $\Delta G^{\gamma\rightarrow\varepsilon}_{Mn}$ | $-1000 + 1.123$ T (J/mol) |
| $\Delta G^{\gamma\rightarrow\varepsilon}_{Cr}$ | 1370–0.163 T (J/mol) |
| $\Delta G^{\gamma\rightarrow\varepsilon}_{Ni}$ | $1046 + 1.255$ T (J/mol) |
| $\Delta G^{\gamma\rightarrow\varepsilon}_{Si}$ | −560–8 T (J/mol) |
| $\Delta G^{\gamma\rightarrow\varepsilon}_{V}$ | $-3500 + 0.7$ T (J/mol) |
| $\Delta G^{\gamma\rightarrow\varepsilon}_{N}$ | [41] |
| $\Delta G^{\gamma\rightarrow\varepsilon}_{FeMnX/C}$ | $\frac{1246}{x_C}(1-\exp(-24.29x_C)) - 17.175x_{Mn}$(J/mol) |
| $\Omega^{\gamma\rightarrow\varepsilon}_{FeMn}$ | $2873 - 717(x_{Fe} - x_{Mn})$(J/mol) |
| $\Omega^{\gamma\rightarrow\varepsilon}_{FeCr}$ | 2095 (J/mol) |
| $\Omega^{\gamma\rightarrow\varepsilon}_{FeNi}$ | 2095 (J/mol) |
| $\Omega^{\gamma\rightarrow\varepsilon}_{FeSi}$ | $2850 + 3520\,(x_{Fe} - x_{Si})$(J/mol) |
| $\Omega^{\gamma\rightarrow\varepsilon}_{CrNi}$ | 4190 (J/mol) |
| $\sigma_s$ | 8 (mJ/m$^2$) |
| $\rho_s$ | $2.94 \times 10^{-5}$ $(mol/m^2)$ |

**Table 3**
SFE values (mJ/m$^2$) of the studied steels calculated at various temperatures based on the Olson-Cohen Thermodynamical approach.

| Steel | Temperature (°C) | | | | |
|---|---|---|---|---|---|
| | RT | 800 | 900 | 1000 | 1100 |
| MnCr-V | 34.2 | 169.1 | 186.8 | 204.4 | 222.1 |
| MnCr-Si-V | 34.7 | 150.3 | 165.4 | 180.5 | 195.6 |

### 3.2. Initial microstructure

Microstructural observations of the studied steels following homogenization and hot rolling (12 mm slab) demonstrate apparent differences in phase composition. The MnCr-V steel displays a completely austenitic structure, marked by the γ-fcc phase. This suggests that the steel retains a uniform austenitic grain structure without substantial Si content, as illustrated in Fig. 1(a). Conversely, the MnCr-Si-V steel reveals a minor presence of δ-ferrite. The microstructural analysis confirms that the sample primarily consists of an austenitic phase, with minor regions of

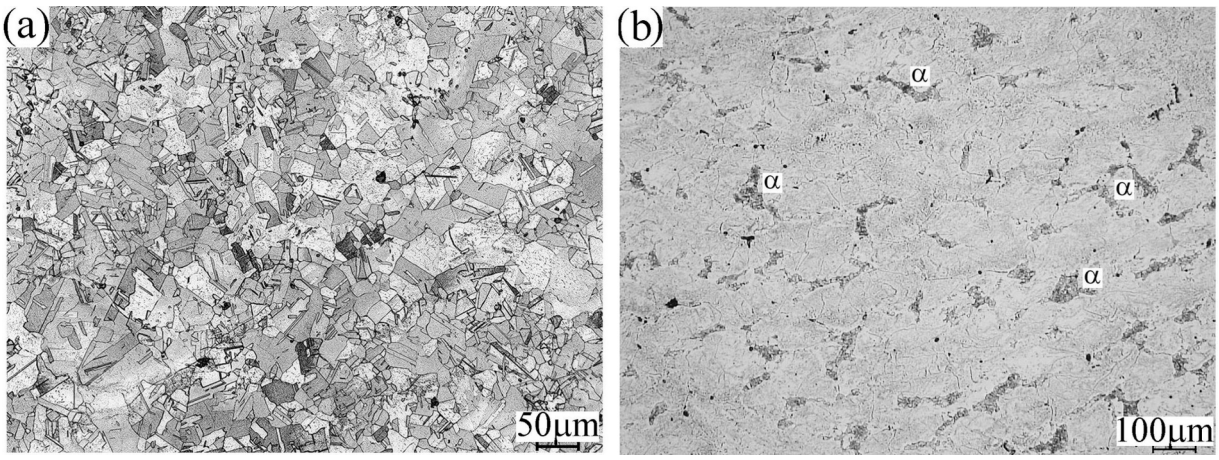


**Fig. 1.** LCSM images depicting the microstructures of the studied steels post-hot rolling: (a) MnCr-V and (b) MnCr-Si-V steel.

skeletal ferrite shown in grey (refer to Fig. 1(b)). The ferrite fraction was measured at around 7 % using the direct comparison method [18].

Fig. S1 illustrates the XRD patterns for MnCr-Si-V and MnCr-V steels following thermomechanical processing. Both alloys display significant diffraction peaks associated with the γ-phase (face-centered cubic, FCC) austenite, particularly the γ-(111), γ-(200), and γ-(220) reflections. However, a distinct δ-(110) peak, indicative of the body-centered cubic (BCC) δ-ferrite phase, is observed only in the MnCr-Si-V steel at approximately 44.7°. The presence of the ferrite peak, although less intense than the austenite peaks, confirms the formation and partial retention of δ-ferrite in the Si-containing alloy. In contrast, the MnCr-V steel exhibits a completely austenitic microstructure, as indicated by the absence of any ferrite-related peaks. These results indicate that the addition of Si promotes δ-ferrite formation and stabilizes its presence, which is consistent with its known ferrite-stabilizing effect in high-alloyed steels.

Overall, this suggests that adding 2.2 wt.% Si is enough to promote the formation of the δ-ferrite phase after quenching to RT.

The low Ms values illustrated in Table 1 emphasize that martensitic transformation is unlikely to occur under the applied processing and cooling conditions. This further supports the interpretation that the observed BCC phase in the high-Si steel is retained δ-ferrite rather than martensite.

### 3.3. Flow behavior at high temperatures

Fig. 2 illustrates typical true (stress–strain) curves for the steels subjected to different hot-deformation conditions. Fig. 2(a) clearly shows that at all temperatures ranging from 950 to 1100 °C and at the low strain rate of 0.1 $s^{-1}$, the flow curves of MnCr-V steel display a peak at strains between 0.1 and 0.25, followed by a gradual decrease in flow stress level. It is widely recognized that the appearance of peak stress ($\sigma_p$) signifies the activation of the DRX mechanism [48–50].

Observation shows that MnCr-V steel with lower Si content exhibits greater flow stress than the higher-Si variant (MnCr-Si-V). For instance, at 950 °C and a low strain rate of 0.1 $s^{-1}$, the flow stresses are 260 and 220 MPa for the MnCr-V and MnCr-Si-V steels, respectively (Fig. 2 (a)). At 1000 °C, the related values of $\sigma_p$ are 210 and 185 MPa. The difference in hot-deformation resistance of the steels appears to decrease at higher temperatures, reaching only 10 MPa at 1100 °C.

Fig. 2(b) shows that both steel types display continuous strain hardening behavior at a higher strain rate of 1 $s^{-1}$. In this case, the flow resistance rises with strain, lacking a distinct $\sigma_p$ at the flow curves. This could indicate that dynamic recovery (DRV) is the primary process, particularly at lower temperatures of 950–1000 °C, during which dislocation annihilation and rearrangement occur. At this strain rate, the MnCr-V steel shows consistently higher flow stress than the MnCr-Si-V

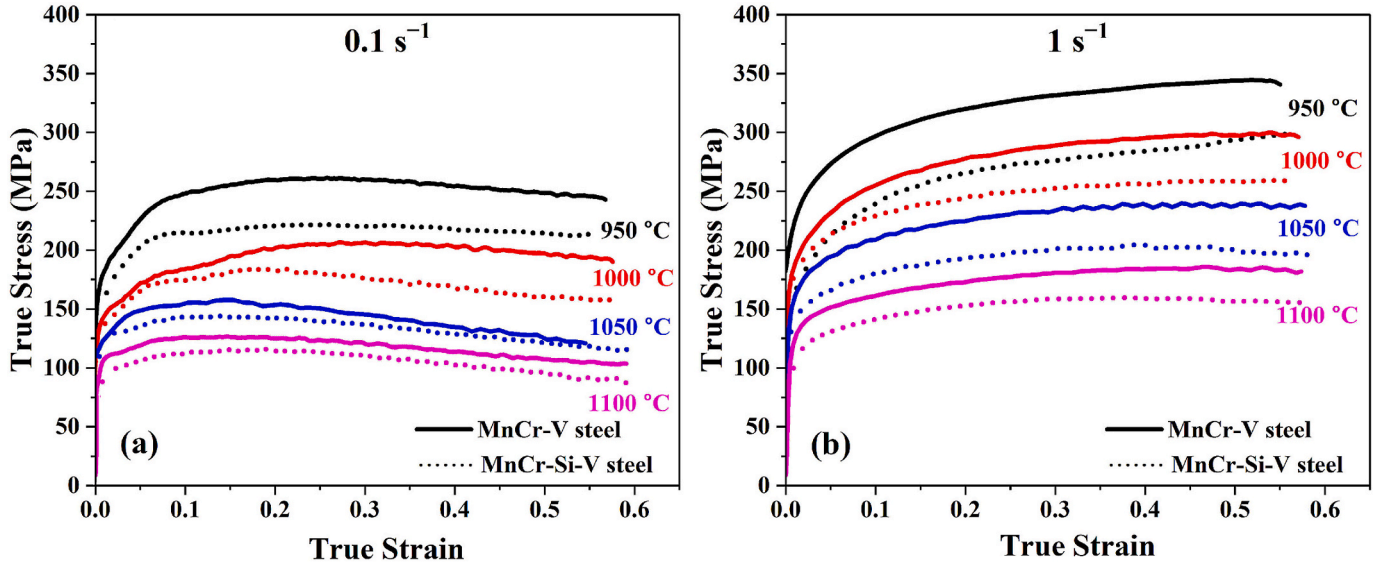


**Fig. 2.** Typical true (stress–strain) curves for the steels across temperatures of 950–1100 °C at strain rates of (a) 0.1 $s^{-1}$ and (b) 1 $s^{-1}$.

steel, highlighting the impact of Si in reducing flow resistance during hot deformation. At 950 °C and a true strain of 0.3, the flow stress of MnCr-V steel is 330 MPa, in contrast to 280 MPa for MnCr-Si-V steel, which is 50 MPa lower.

At a temperature of 1100 °C, the flow stress of both steels decreases because of increased softening at high temperatures, which is driven by DRX, even in the absence of $\sigma_p$(see Section 3.4.). The ferrite phase in MnCr-Si-V steel contributes to lower flow resistance at this temperature. The stress levels for MnCr-V and MnCr-Si-V steels decrease to 180 MPa and 160 MPa, respectively. At 1100 °C, the flow stress difference between the two steels is around 20 MPa, slightly greater than at lower strain rates.

It has been established that the hot-deformation parameters can be expressed through the Zener–Hollomon parameter (Z), which characterizes the impact of temperature T and strain rate $\dot{\varepsilon}$ on the deformation behavior, as described by McQueen and Ryan. [51],

$$Z = A\{sinh(\alpha\sigma_p)\}^n = \dot{\varepsilon} exp\left(\frac{Q_{HD}}{RT}\right) \quad (4)$$

where α represents the stress multiplier, and n is the stress exponent. A is a material constant, R is the universal gas constant, and T is the absolute deformation temperature. The activation energy $Q_{HD}$ of hot deformation of the studied steels was estimated by the following relationship at constant strain and strain rate [52,53]:

$$Q_{HD} = Rn\left[\frac{ln[sinh(\alpha\sigma_p)]}{\frac{1}{T}}\right]_{\dot{\varepsilon}} \quad (5)$$

By analyzing the dependence of the $\sigma_p$ on T and $\dot{\varepsilon}$, it can be inferred that the $Q_{HD}$ is 507 kJ/mol for the MnCr-V steel, which is higher than $Q_{HD}$ of 447 kJ/mol for the MnCr-Si-V steel. Table 4 lists the $Q_{HD}$ of the studied steels compared to high-Mn TWIP and austenitic stainless steels.

The present study reveals that adding 2.2 % Si reduces both the hot-deformation resistance and the $Q_{HD}$. This behavior contrasts with that observed in high-Mn TWIP steels, such as 25Mn3Al, where the inclusion of 3 % Si was reported to increase both the hot-deformation resistance and $Q_{HD}$, from 365 to 406 kJ/mol, as shown in Ref. [29]. It is important to note that both 25Mn3Al and 25Mn3Si3Al steels exhibit a fully austenitic structure across the studied deformation temperature range (800–1100 °C). The increased flow resistance and $Q_{HD}$ in the 25Mn3Si3Al steel can be attributed to the solid-solution strengthening effect of Si and the solute drag effect, which impedes dislocation glide within the fully austenitic matrix [46]. In contrast, the addition of 2.2 wt.% Si in the present 10 % Mn steel promotes the formation of the ferrite phase at high temperatures, as evidenced in Fig. 1 and discussed in Section 3.4. At elevated temperatures, ferrite is significantly softer than the austenitic matrix, reducing the $\sigma_p$ and $Q_{HD}$. For instance, in a low-alloyed Fe-C-Mn-Si steel, the $Q_{HD}$ of ferrite has been reported to be substantially lower (256 kJ/mol) than that of austenite [30]. Our previous studies highlighted a significant impact of the microstructural phases on the $Q_{HD}$ in Fe-Mn-Al-Si alloys [54,57,58]. In Fe-23Mn-8Al-0.5Si, the presence of δ-bcc structure contributed to a substantial reduction in $Q_{HD}$, lowering it to approximately 300 kJ/mol. This reduction is attributed to the softer nature of the ferrite phase, which facilitates dislocation motion and promotes DRV over DRX during deformation. Conversely, in Fe-24Mn-3Al-0.5Si, which features a fully austenitic structure without the δ-ferrite, the $Q_{HD}$ was measured at a higher value of ~ 400 kJ/mol. The absence of the softer δ-bcc phase results in a deformation process dominated by the harder γ-fcc matrix, where dislocation interactions and the onset of DRX require higher energy. These results highlight the essential impact of phase composition on deformation mechanisms and energy needs, providing valuable insights for optimizing alloy design in processing scenarios.

**Table 4**
Activation energy for hot deformation ($Q_{HD}$) of the current steels, along with values from the literature for other high-Mn TWIP and austenitic stainless steels for comparison.

| Steel | $Q_{HD}$ kJ/mol | Ref. |
|---|---|---|
| MnCr-V | 507 | Present work |
| MnCr-Si-V | 447 | Present work |
| 25Mn3Al | 397 | [54] |
| 25Mn3Al | 365 | [29] |
| 25Mn3Si3Al | 406 | [29] |
| 22Mn1.5Al1.5Si0.4C0.12 V | 446 | [52] |
| 304LN | 473 | [55] |
| 316L | 465 | [56] |

Phase stability and equilibrium predictions were performed to evaluate the stability range of the phases at high temperatures in both steels. Thermo-Calc simulations were conducted using Thermo-Calc software version 2025a with the TCFE13 thermodynamic database. The precise chemical compositions of the steels were utilized to ensure accurate predictions of phase fractions and transformation predictions.

Figs. S2 and S3 show the equilibrium phase diagrams for MnCr-Si-V and MnCr-V steels. The Thermo-Calc simulation results reveal that the δ-ferrite BCC phase becomes thermodynamically stable at temperatures exceeding roughly 1030 °C in the MnCr-Si-V steel, maintaining a considerable volume fraction until it reaches the liquidus temperature (~1380 °C). In contrast, for the MnCr-V steel, δ-ferrite disappears entirely at temperatures below approximately **1240 °C**, as predicted by Thermo-Calc. Therefore, during hot rolling thermomechanical processing in the temperature range of 1200–1100 °C, the MnCr-V steel undergoes complete transformation to austenite, resulting in a fully austenitic microstructure after fast cooling from the deformation temperature to RT. On the other hand, the MnCr-Si-V steel, containing 2.22 wt.% Si maintains δ-ferrite stability over a broader temperature range (1380–1030 °C). As a result, a fraction of ~ 0.1 δ-ferrite is retained in the final microstructure after fast cooling due to insufficient time for complete diffusion-driven transformation to austenite. These findings correlate well with the experimental XRD. To suppress δ-ferrite formation and improve mechanical properties, strategies such as adjusting solution annealing temperatures just below the ferrite solvus and employing controlled cooling rates post-deformation can be applied. These thermodynamic and process-based insights provide a foundation for optimizing the phase balance and microstructure of V-microalloyed MnCr stainless steels.

### 3.4. Microstructural evolution during hot deformation

The behavior of the flow stress curves is a crucial indicator of the underlying hot-deformation mechanisms, such as DRV and DRX, and texture promotion at elevated temperatures. These mechanisms are mainly influenced by three factors: T, $\dot{\varepsilon}$, and $\varepsilon$ [58]. We examined the microstructures of specimens after hot-compression experiments using the EBSD technique to investigate the softening mechanisms and their effects on the flow stress differences between the steels.

At a deformation temperature of 1100 °C and a strain rate of 1 $s^{-1}$, DRX is significantly enhanced, resulting in a microstructure that is approximately 80 % recrystallized with fine, equiaxed grains, as shown in Fig. 3(a). It's important to note that this pronounced DRX takes place despite the flow curves at 1 $s^{-1}$ being flat and lacking a distinct peak stress region (Fig. 2(b)).

Fig. 3(a) also shows that the fraction of high-angle grain boundaries (HAGBs), marked in blue, rises notably to 55 %. This surge in HAGBs results from the necklacing mechanism of DRX, which involves the formation of new grains mainly at the edges of previously deformed grains, forming a necklace-like arrangement surrounding larger grains. This process is well-documented in existing literature [59–61]. Despite the high temperature of 1100 °C, few non-recrystallized large grains, labeled A, B, and C, remained. This may be due to the high strain rate of 1 $s^{-1}$, which could limit the time available for the complete

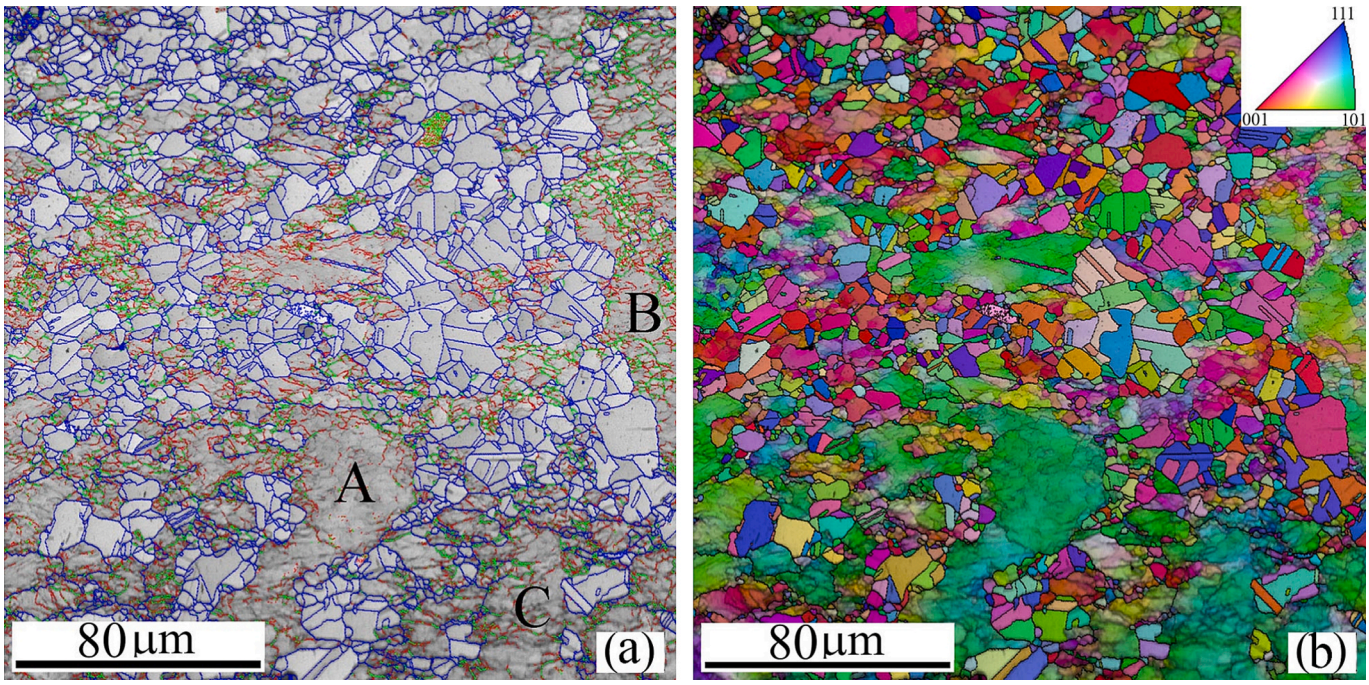


**Fig. 3.** Microstructures of hot deformed MnCr-V steel at 1100 °C/1 $s^{-1}$ with a strain of 0.6. (a) EBSD grain boundary map of (a) (low-angle boundaries from 2° to 5° shown in red, from 5° to 15° in green, and high-angle boundaries > 15° in blue), (b) IPF map illustrating the grain structure in (a).

recrystallization of all grains. DRX is a thermally activated diffusion-controlled process that depends on the rate of atomic diffusion, the movement of grain or subgrain boundaries, and dislocation movement [58,62]. At higher strain rates, the time required for atomic diffusion and boundary migration is reduced, resulting in incomplete DRX, even at elevated temperatures. Therefore, although the temperature reaches a sufficient level at 1100 °C, the rapid deformation at 1 $s^{-1}$ may hinder complete DRX. Hamada et al. [63] reported similar findings in austenitic high-Mn TWIP steels, noting that incomplete DRX occurred at high strain rates, even at elevated temperatures. This emphasizes the essential harmony among temperature, strain rate, and deformation mechanisms to achieve the intended microstructural transformations.

The corresponding orientation map in Fig. 3(b) further highlights the differences in crystallographic orientation between the newly formed and non-recrystallized grains. Likewise, at lower temperatures, the newly recrystallized fine grains primarily show the ⟨001⟩ orientation, indicating their fresh formation and alignment during the recrystallization process. Conversely, the larger, coarse austenite grains that have not undergone recrystallization exhibit a ⟨101⟩ crystallographic orientation. This specific orientation emphasizes the incomplete extent of the DRX occurring under the current conditions. The variations in orientation highlight how hot-deformation factors, including temperature and strain rate, influence the microstructural development of steel, as shown in Fig. 3(b). The disparity in crystallographic orientations between newly recrystallized and parent grains has been well reported [64]. This occurs because the nucleation and growth processes of the new grains favor an orientation that differs from the original grains, along with variations in dislocation density. [65].

Fig. 4 displays a representative microstructure of the hot-deformed MnCr-Si-V steel processed at 1000 °C and a strain rate of 0.1 $s^{-1}$. The misorientation boundary map illustrated in Fig. 4(a) shows a partially recrystallized structure featuring fine grains distributed among the boundaries of large, elongated, and deformed grains. The fraction of DRX grains is approximately 25 %, showing no significant difference compared to the MnCr-V steel under identical conditions, see Fig. 3. However, a striking feature of the microstructure is the coexistence of ferrite within the austenitic matrix. The significant presence of ferrite indicates that it has been retained from the previous annealing stage at 1200 °C. This observation aligns with the Thermo-Calc prediction, which shows that ferrite is stable at temperatures ≥ 1030 °C (further discussed in Section 3.5). The presence of ferrite, even at temperatures of 1000 °C and likely at 950 °C due to the prior 1200 °C annealing, accounts for the reduction in flow stress by 2.2 wt.% Si alloying. The misorientation map illustrates the stark contrast in strain between ferrite and austenite, with ferritic grains appearing lighter and austenitic grains darker, reflecting their different grey-scale levels. The retention of ferrite at 1000 °C is crucial for deformation behavior, as its softer characteristics compared to austenite lead to the decreased flow stress seen in the 2.2 wt.% Si alloyed steel.

Within the austenitic matrix, the necklacing mechanism facilitated the development of a partially DRXed structure, while the ferrite phase predominantly displayed a subgrain structure defined by low-angle grain boundaries (LAGBs), as shown in Fig. 4(a). This difference in the grain boundary characteristics results from the rapid recovery in ferrite, facilitated by its high SFE [66]. Fig. 4(b) presents the phase map, depicting islands of flattened ferrite (green) that project perpendicularly to the deformation direction. This behavior stems from the ferrite phase's significant plasticity and its low resistance to elevated temperature deformation. Fig. 4(c) illustrates the crystallographic orientation of the austenite matrix formed during deformation at 1000 °C/0.1 $s^{-1}$. The map features subgrains in various colors, representing distinct orientations and misorientation angles ranging from 10° to 15°. A closer look at grain A, marked in Fig. 4(c), is provided in Fig. 4(d). This zoomed-in perspective highlights intricate features like the serrated grain boundary shapes that encourage mechanisms of bulging and necklacing. The identified serrations and bulging along the grain boundaries serve as nucleation sites for new DRX grains.

The high Si addition plays a significant role in influencing both ferrite phase formation and the DRX behavior of the studied steels during hot deformation. Si is a known ferrite stabilizer, and its presence shifts the ferrite–austenite equilibrium, promoting the formation and retention of δ-ferrite at high temperatures. This is supported by Thermo-Calc predictions, which show δ-ferrite stability above ~ 1030 °C in the high-Si steel. Furthermore, Si affects DRX kinetics through two primary

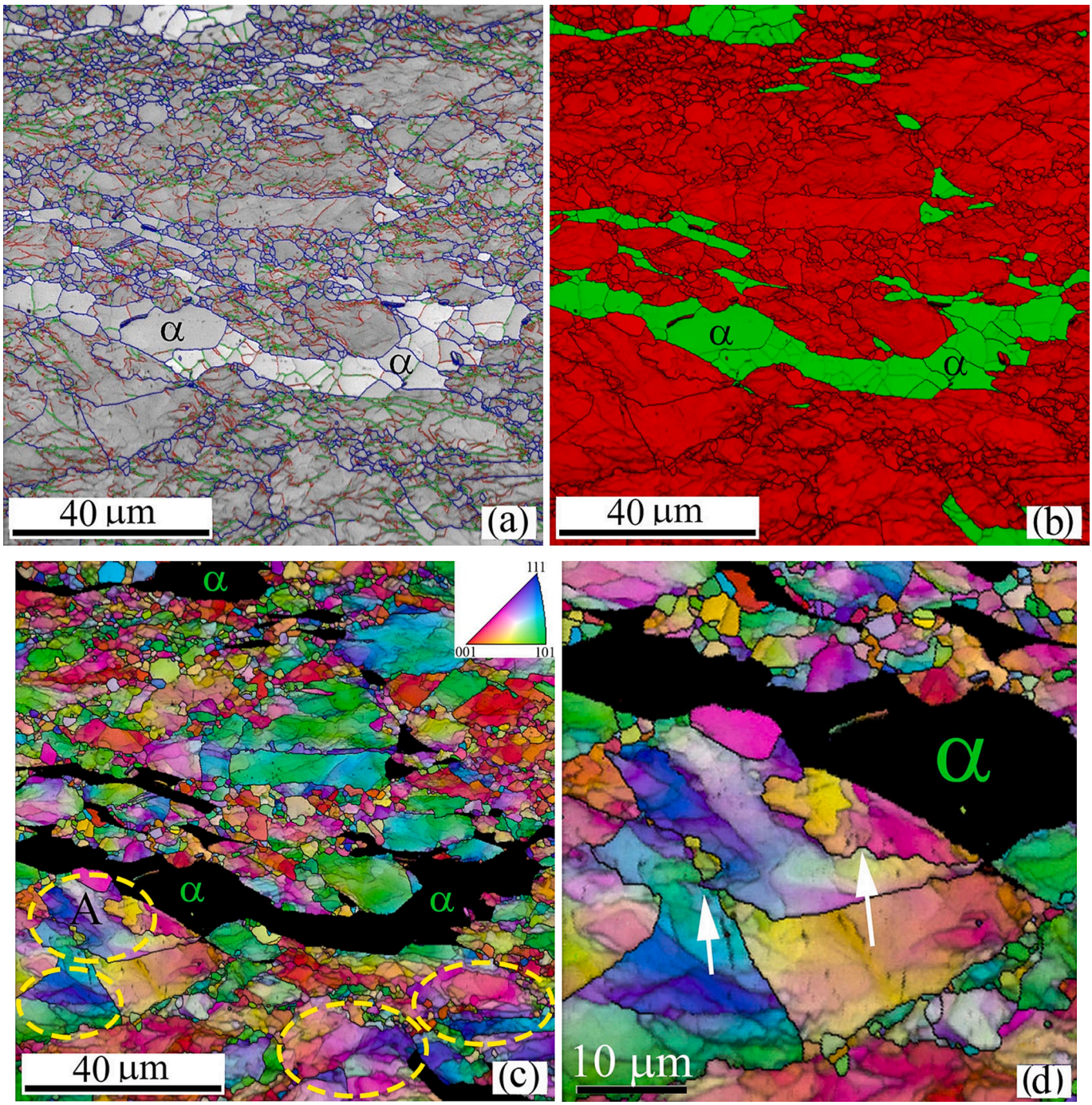


**Fig. 4.** Microstructures of MnCr-Si-V steel under hot compression at 1000 °C/0.1 $s^{-1}$ to a strain of 0.6. (a) EBSD grain boundary map showing low-angle boundaries (2° to 5° in red), medium-angle boundaries (5° to 15° in green), and high-angle boundaries (>15° in blue), (b) the corresponding phase map, (c) the Inverse Pole Figure (IPF) map of austenitic grains displayed in (a), and (d) a close-up view of grain A from (c).

mechanisms: it alters the SFE and introduces solute drag effects. The high-Si steel demonstrates slightly lower DRX fractions at elevated temperatures compared to its low-Si counterpart, particularly at intermediate temperatures such as 1000 °C. This behavior is attributed to Si-induced solute drag, which hinders grain boundary migration and postpones the progress of DRX. As the deformation temperature rises, atomic mobility enhances and overcomes this drag effect, allowing for more complete recrystallization. These combined effects of Si on phase stability and recrystallization kinetics emphasize its crucial role in influencing microstructural evolution during thermomechanical processing.

As the deformation temperature increased to 1100 °C, the DRX mechanism became predominant, even at a strain rate of 1 $s^{-1}$. Fig. 5(a) illustrates a fully recrystallized austenitic matrix with an average grain size of 3.4 μm. A notable feature of the grain boundary map in Fig. 5(a) is the presence of LAGBs at the lowest fraction of 0.16. It is well documented that more slip systems can be activated at higher deformation temperatures, resulting in more uniform deformation. Consequently, the DRX softening mechanism becomes effective, leading to the partial consumption of LAGBs and their replacement by newly recrystallized fine grains [67]. The ferrite phase has experienced DRX at the elevated strain rate, as evidenced by HAGBs within the grains. Moreover, there is

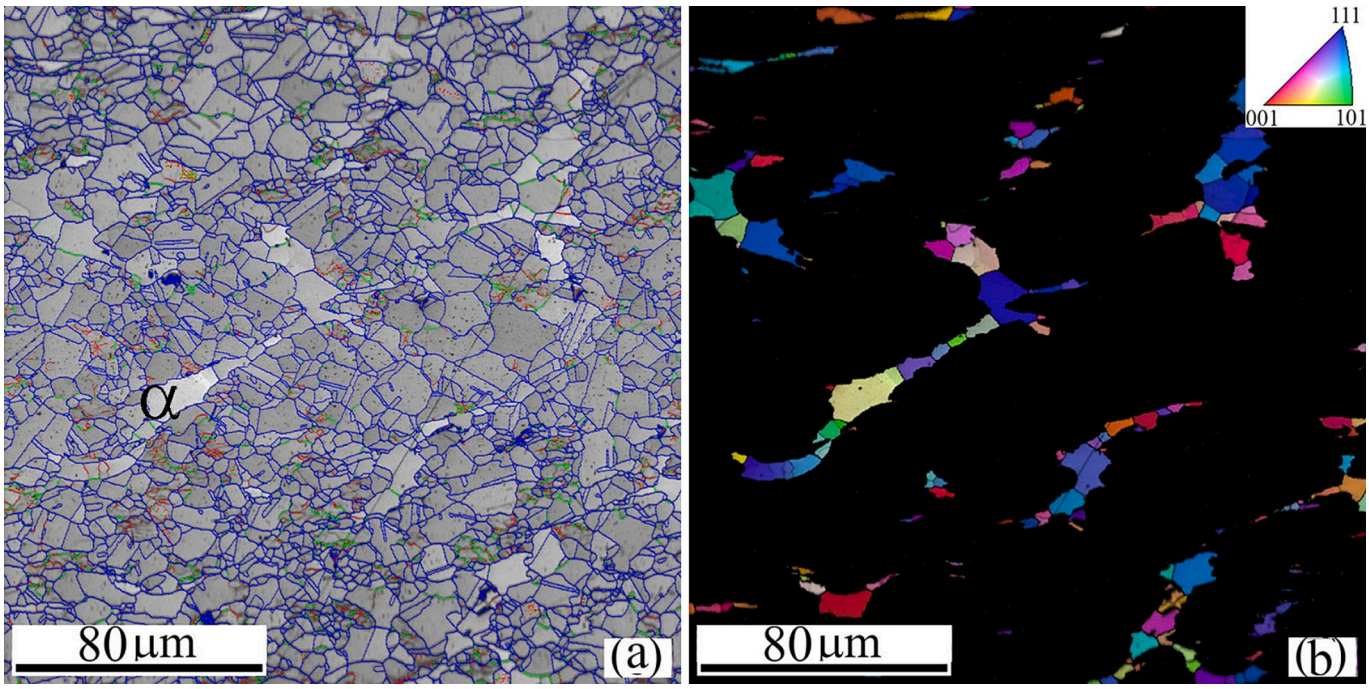


**Fig. 5.** Hot compressed microstructures of MnCr-S-V steel at 1100 °C/1 $s^{-1}$ to a strain of 0.6. (a) EBSD-boundary map, and (d) IPF map of the ferritic grains in (a).

a rise in dislocation density and stored energy, further enhancing the likelihood of the ferrite phase undergoing DRX. The literature extensively documents the increased tendency for DRX in the ferrite phase at elevated strain rates [58,68]. Fig. 5(b) presents a detailed orientation map of the ferrite phase, emphasizing the crystallographic orientation of the ferrite grains while omitting the austenitic grains for better clarity. Most of the ferrite grains exhibit a ⟨111⟩ orientation, which is shown in blue on the map. This dominance of the ⟨111⟩ orientation indicates that the ferrite grains have experienced significant reorganization and alignment due to the DRX process.

Phase maps from EBSD of the hot-deformed microstructures reveal the presence of δ-ferrite and enable quantification at varying deformation temperatures. Ferrite fractions were estimated at approximately 7.5 % at 950 °C and 9.6 % at 1100 °C. These figures suggest only minor temperature variations, which align with expectations due to the rapid hot deformation time frame that limits the diffusion-controlled ferrite-to-austenite transformation. The observed δ-ferrite predominantly comes from the initial hot-rolled slabs, with minimal new ferrite formed during deformation. Although the difference in volume fraction is relatively small, the continual presence of δ-ferrite as a soft phase contributes to lower flow stress in high-Si steel. This effect is more pronounced at elevated temperatures, where the slight increase in ferrite fraction, combined with its reduced resistance to deformation, clarifies the softer flow behavior compared to low-Si steel. These results emphasize the importance of δ-ferrite in softening the high-temperature deformation response.

While it is reasonable to believe that higher deformation temperatures could enhance the presence of soft δ-ferrite, accurately measuring the ferrite fraction during hot deformation remains challenging. This difficulty arises from the rapid, diffusion-controlled transition of ferrite to austenite as the material cools from the deformation temperature to RT [69]. Consequently, the ferrite fraction observed at RT is likely lower than the actual amount present during deformation. However, EBSD analysis of the deformed microstructures reveals a small but consistent retention of δ-ferrite, helping to soften the flow behavior, especially at elevated temperatures.

As shown by Thermo-Calc phase diagrams (Fig. S2-S3) and EBSD analyses (Figs. 4 and 5), the MnCr-Si-V steel contains a fraction of δ-ferrite, particularly at high temperatures (>1030 °C). However, the volume fraction of ferrite is relatively low compared to austenite. Therefore, the calculated $Q_{HD}$ primarily reflects the dominant deformation behavior of the austenitic matrix. Nevertheless, the presence of δ-ferrite may slightly reduce the measured $Q_{HD}$ by facilitating softening mechanisms such as DRV within the ferrite phase.

This conclusion is consistent with the low $Q_{HD}$ value of the high-Si steel (~447 kJ/mol) compared to that of their low-Si counterparts (~507 kJ/mol). This reduction is due to the presence of soft δ-ferrite, which undergoes easier recovery at high temperatures, thereby lowering the overall energy required for hot deformation.

Regarding recrystallization, the δ-ferrite phase can indeed undergo fast DRV and, to a lesser extent, continuous dynamic recrystallization (CDRX) during thermomechanical processing. The EBSD analysis revealed that ferrite regions predominantly contain low-angle grain boundaries (LAGBs) after deformation, suggesting that DRV occurs more readily in ferrite compared to austenite under the same conditions. This is due to the inherently higher SFE and faster dislocation annihilation rates in ferrite; thus, the mechanism is dominated by recovery rather than the classical discontinuous dynamic recrystallization (DDRX) observed in austenite.

Further experimental studies involving controlled variations in the deformation parameters, i.e., temperature, holding time, and cooling rate, would be valuable to fully characterize the transformation and recrystallization behavior of the BCC phase during thermomechanical processing.

### 3.5. Hot-deformation processing maps

A processing map was constructed using dynamic material model (DMM) concepts to assess the hot workability properties of 10Mn-18Cr TWIP-type stainless steel with two different Si contents (0.4 and 2.2 wt. %). Consequently, modifications in the microstructure (*J* co-content) accounted for a minor portion of the instantaneous dissipation of the total power (*P*), which was caused mainly by an increase in temperature (*G* Content). One way to express the dissipation of power is as follows:

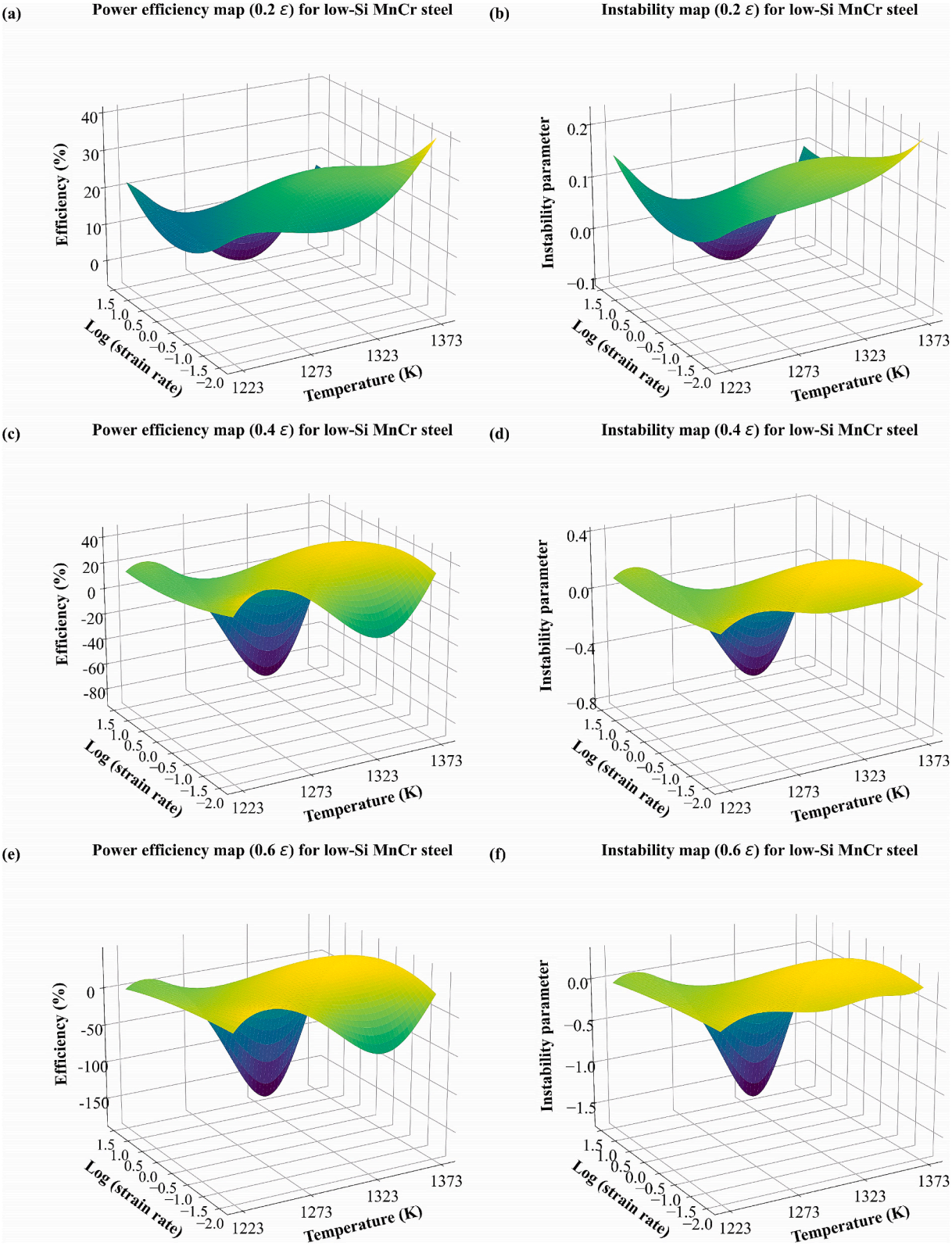


**Fig. 6.** 3D maps showing power dissipation efficiency and instability for MnCr-V steel at various true strains: (a, b) at 0.2 strain, (c, d) at 0.4 strain, (e, f) at 0.6 strain.

$$P = \sigma.\dot{\varepsilon} = \int_0^{\dot{\varepsilon}} \sigma.d\dot{\varepsilon} + \int_0^{\sigma} \dot{\varepsilon}.d\sigma = G + J \tag{6}$$

The strain-rate sensitivity (m), defined as follows, establishes the power that separates the G and J co-contents:

$$m = \frac{\Delta J}{\Delta G} = \frac{\dot{\varepsilon}.d\sigma}{\sigma.d\dot{\varepsilon}} = \frac{d(ln\sigma)}{d(ln\dot{\varepsilon})_{T,\varepsilon}} \tag{7}$$

When temperature and strain are specified, the J co-content is described as follows:

$$J = \left(\sigma.\dot{\varepsilon}.\frac{m}{m+1}\right) \tag{8}$$

The non-linear dissipator of the workpiece, denoted as J co-content, is normalized with the co-content of a standard linear dissipator (where m = 1). This normalization results in a dimensionless parameter known as the efficiency of power dissipation ($\eta$), which can be expressed as:

$$\eta = \frac{J}{J_{max}} = \frac{2m}{m+1} \tag{9}$$

$\eta$, distinct from process efficiency, refers to a material's ability to disperse power through specific metallurgical processes. The power dissipation map is established at a constant $\varepsilon$ by utilising the variation in $\eta$ as a function of $T$ and $\dot{\varepsilon}$. This map also depicts the constitutive behavior of the material. Depending on the values of $\eta$, a three-dimensional (3D) power dissipation map that is displayed as a function of $T$ and $\dot{\varepsilon}$ may contain hills and valleys. Furthermore, the power-dissipation map, which frequently displays peak efficiency values near the centres of the deterministic domains, may be better represented by a two-dimensional (2D) iso-efficiency contour map. Deterministic domains can be formed according to their morphologies and peak efficiencies, linked to specific microstructural evolutions. In 3D power dissipation maps, they appear as hills, separated by bifurcation regimes represented as valleys.

Prasad et al. [70] developed a continuous criterion using the extremum principles of irreversible thermodynamics to identify the flow instability regimes in the temperature–strain rate space, as applied to the extensive plastic flow outlined by Ziegler et al. [71].

$$\xi(\dot{\varepsilon}) = \frac{\partial \ln\left(\frac{m}{m+1}\right)}{\partial ln\dot{\varepsilon}} + m < 0 \tag{10}$$

The areas of flow instability can be defined by creating an instability map on the power-dissipation map based on the deviation of the instability parameter, $\xi(\dot{\varepsilon})$, with respect to strain rate and temperature. The regime where flow instabilities are expected to occur is the deformation space, where $\xi(\dot{\varepsilon}) < 0$. Moreover, microstructural characterisation was used to validate the deformation mechanisms associated with particular domains/regimes.

The evaluation of $\eta$ and $\xi(\dot{\varepsilon})$ was performed by means of the interpolation of the cubic splines of log ($\sigma$) vs. log $\dot{\varepsilon}$ at each temperature, as outlined in our earlier work [72]. Next, for a specific real strain, the value of $\eta$ was computed as a function of temperature and strain rate (Eq. (9)). Contour maps for 2D *iso*-efficiency and 3D power dissipation were created using the computed $\eta$ values. Furthermore, an instability map

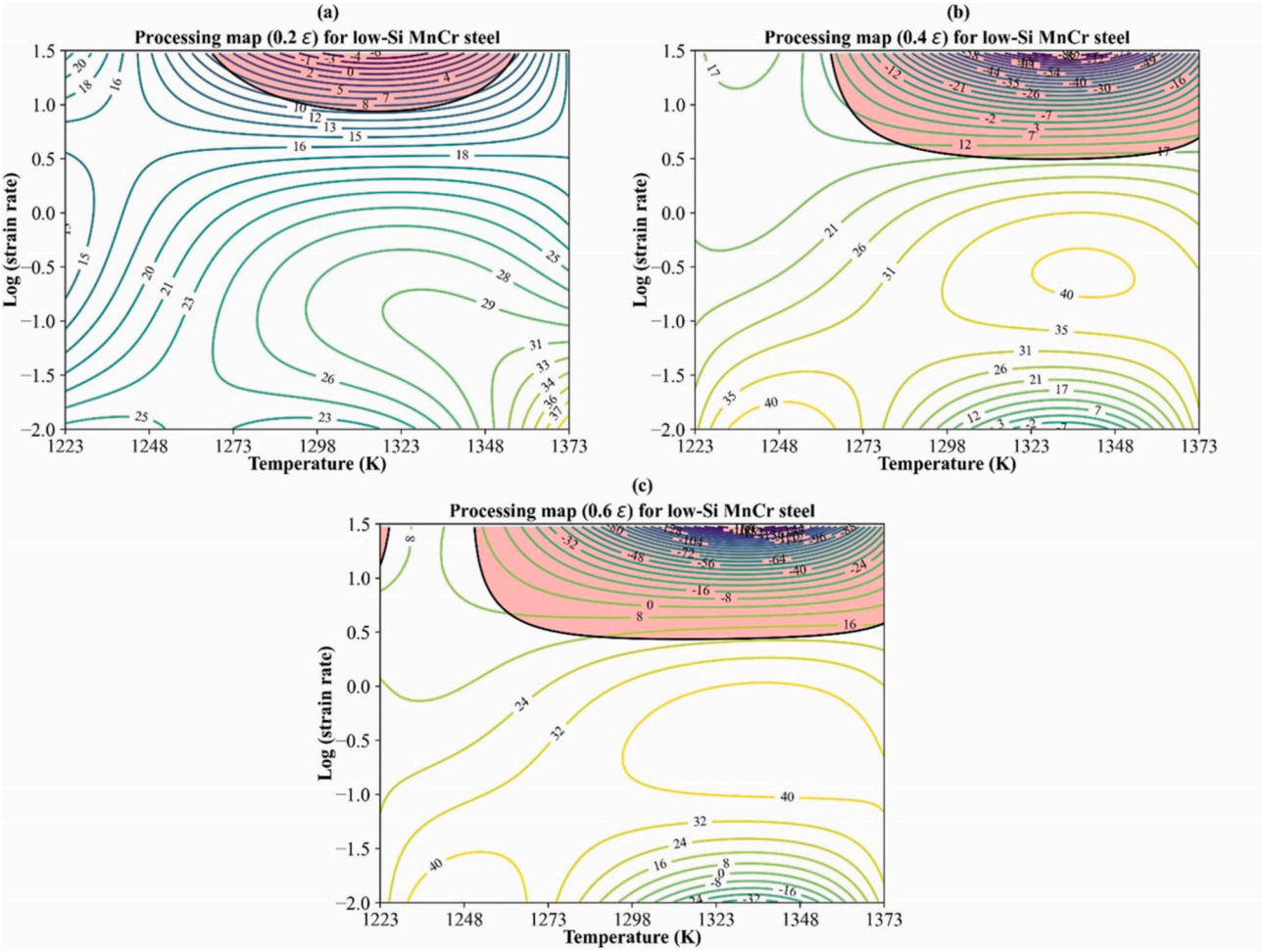


**Fig. 7.** Processing maps for the MnCr-V steel alloy at various true strains: (a) 0.2 strain, (b) 0.4 strain, and (c) 0.6 strain. The red zone indicates the instability regime.

was created for a specific strain by evaluating the $\xi(\dot{\varepsilon})$ parameter as a function of temperature and strain rate (Eq. (10)).

Fig. 6 (a, c, and e) presents the 3D maps of power dissipation efficiency for the MnCr-V steel alloy at true strains of 0.2, 0.4, and 0.6, encompassing various strain rates and temperature ranges. Fig. 6 (b, d, and f) depicts the 3D plots illustrating the instability maps for these specific scenarios. Finally, the processing maps are generated in Fig. 7 (a, b, and c) by overlaying the instability map onto the power-dissipation map.

The processing maps were examined to identify and interpret various

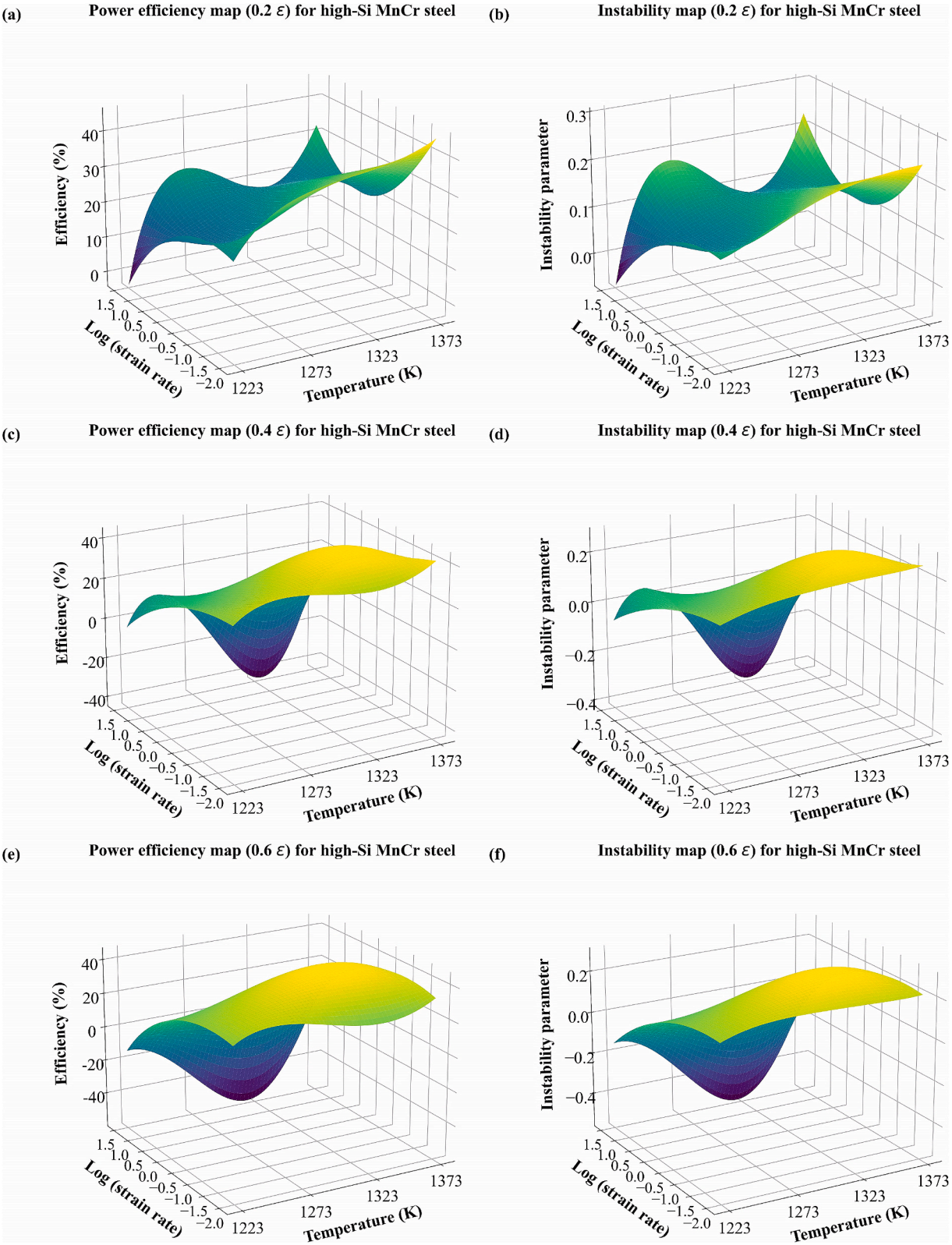


**Fig. 8.** 3D power dissipation efficiency maps and the corresponding 3D instability maps of MnCr-Si-V steel at different true strains, respectively: (a; b) 0.2 strain, (c; d) 0.4 strain, (e; f) 0.6 strain.

deterministic regions and areas of low efficiency concerning power dissipation efficiencies and possible microstructural mechanisms. Likewise, instability regimes were developed and substantiated concerning instability expressions. In contrast, the power dissipation efficiency linked to the cracking process is typically high due to the effective conversion of deformation energy into surface energy. The DRX process demonstrates comparatively low efficiency (< 50 %), with peak power dissipation efficiencies that are usually nearly equivalent or situated closely within a specific strain range in the temperature-strain rate region. Superplastic deformation, characterized by heightened elongation at elevated temperatures and low strain rates, is observed during specific conditions. This phenomenon typically manifests at strain rates that are significantly lower than those found in the DRX process. Additionally, the efficiency of power dissipation often exceeds 60 % [73]. Adiabatic shear bands are expected to form at high strain rates and low temperatures, with instabilities manifesting as strong bands, often accompanied by cracks or voids [74,75]. In contrast, wedge cracks typically nucleate at grain boundaries (GBs), especially at triple points [76], at elevated temperatures, and low strain rates. As a result, hot working is deemed "unsafe" in these areas of the processing map.

In contrast, deterministic processing domains like DRX, DRV, and superplasticity are considered "safe" areas. Superplasticity can cause micropores to form along grain boundaries at higher strains, making processing that involves superplasticity deemed safer for lower strains [77]. Fig. 8 illustrates the processing maps for the MnCr-V steel alloy, constructed at strain levels of 0.2, 0.4, and 0.6, within the compression temperature range of 1223–1373 K and a strain rate of 0.01–10 $s^{-1}$. Every curve represents consistent efficiency, whereas areas of instability are highlighted in red.

Up to strain of 0.6, the MnCr-V steel alloy map in Fig. 7 (c) shows two domains: (1) DRV is represented by the domain in the temperature range of 1223–1273 K and strain rate range of 0.01–0.03 $s^{-1}$, with a peak efficiency of 40 % occurring at 1248 K and 0.01 $s^{-1}$. When DRX initiates, borders with a misorientation angle exceeding 15° appear serrated or bulged. (2) The DRX process occurs within a temperature range of 1298–1373 K and a strain rate range of 0.1–1 $s^{-1}$, achieving peak efficiency of 40 % at 1348 K and a strain rate of 1 $s^{-1}$. The GBs experienced changes due to DRX, leading to an 80 % recrystallized structure characterized by finely equiaxed grains. The material exhibits flow instabilities when strain rates exceed 3 $s^{-1}$ and within the temperature range of 1248–1373 K. Furthermore, a minor area of instability exists at strain rates exceeding 15 $s^{-1}$ within the temperature range of 1223–1227 K. This results in flow localization. For strains up to 0.4, the MnCr-V steel alloy map (Fig. 7 (b)) exhibits two key domains: (1) DRV is featured within the temperature range of 1223–1273 K and a strain rate of 0.01–0.03 $s^{-1}$, achieving a peak efficiency of 40 % at 1248 K and 0.01 $s^{-1}$. (2) DRX is observed in the temperature range of 1298–1373 K and a strain rate of 0.01–1 $s^{-1}$, with a maximum efficiency of 40 % occurring at 1348 K and 0.01 $s^{-1}$.

The material exhibits flow instabilities at strain rates exceeding 3 $s^{-1}$ and within the temperature range of 1260–1373 K. This results in flow localization [78]. For strain levels up to 0.2, the MnCr-V steel map (refer to Fig. 7 (a)) illustrates two key domains: (1) DRV, found in the temperature range of 1223–1230 K, and strain rates of 0.2–3.2 $s^{-1}$, with peak efficiency reaching 15 % at 1223 K and 3 $s^{-1}$. (2) DRX, observed within the temperature range of 1260–1373 K and strain rates of 0.01–1

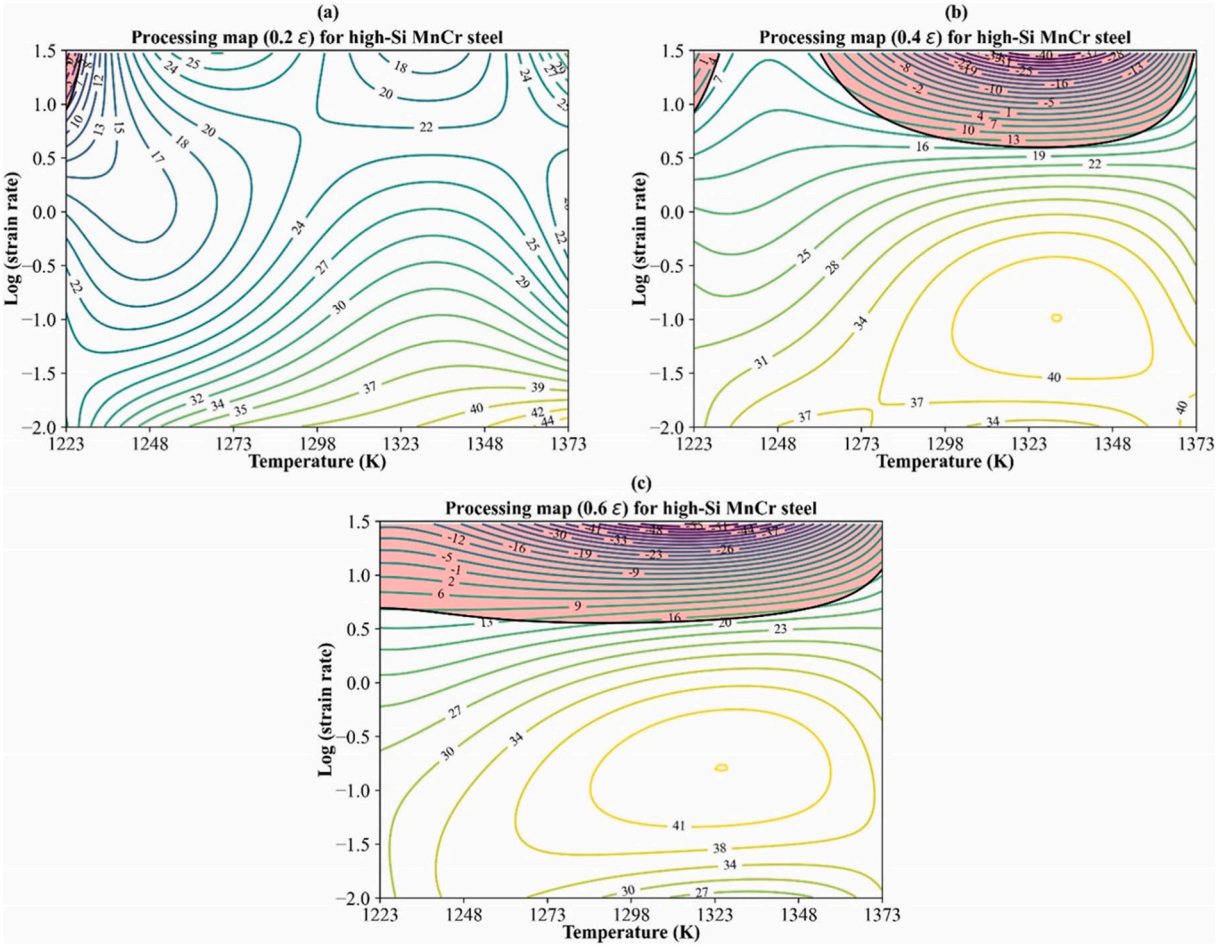


**Fig. 9.** Processing maps for the MnCr-Si-V steel alloy at various true strains: (a) ε = 0.2, (b) ε = 0.4, and (c) ε = 0.6. The instability regime is indicated in the red zone.

$s^{-1}$, achieving maximum efficiency of 37 % at 1373 K and 0.01 $s^{-1}$. Beyond approximately 10 $s^{-1}$ strain rates, within the temperature span of 1265–1355 K, the material demonstrates flow instabilities, resulting in a localized flow.

Furthermore, it was observed that the deterministic domains supporting stable flow exhibited relatively high $\eta$–values, predominantly occurring in low-Z conditions where deformation heating is minimized at low strain rates, allowing sufficient time for dislocation motion. In contrast, the instability regimes were linked to high-Z conditions. Conversely, for high-strain-rate processes that lead to flow localization, adiabatic heat cannot be transferred quickly under high-Z conditions. The MnCr-V steel alloy can be processed safely at a reasonably high $\eta$-value, avoiding instability, and it has good inherent workability within the safe workable domains.

Similarly, Fig. 8 (a, c, and e) presents the 3D power dissipation efficiency maps created for the MnCr-Si-V steel alloy at true strains of 0.2, 0.4, and 0.6, encompassing the strain rate and temperature ranges. The 3D plots of the instability maps for the respective cases are displayed in Fig. 8 (b, d, and f). The processing maps are ultimately produced in Fig. 9 (a, b, and c) by overlaying the instability map onto the power-dissipation map.

For strains up to 0.6, the MnCr-Si-V steel alloy map (Fig. 9 (c)) displays two distinct domains: (1) The first domain indicates DRV, occurring within the temperature range of 1223–1373 K and a strain rate between 0.01 and 1 $s^{-1}$, achieving peak efficiency of 34 % at 1323 K and 0.01 $s^{-1}$. The conditions at 1223 K and these strain rates are insufficient for complete DRX. (2) The second domain signifies DRX, observed in the temperature range of 1260–1373 K, and a strain rate from 0.03 to 1 $s^{-1}$, where the maximum efficiency reaches 41 % at 1323 K and 0.1 $s^{-1}$.

When strain rates exceed about 3 $s^{-1}$ and temperatures are between 1223 and 1373 K, the material exhibits flow instabilities, resulting in flow localization [79].

For a strain of up to 0.4, the MnCr-Si-V steel alloy map (Fig. 9 (b)) reveals two distinct domains: (1) The DRV domain spans the temperature range of 1223–1373 K and strain rates from 0.01 to 1 $s^{-1}$, peaking in efficiency at 34 % at 1323 K and 0.01 $s^{-1}$. (2) The DRX domain covers temperatures between 1268 K and 1360 K with strain rates of 0.03 to 0.3 $s^{-1}$, achieving maximum efficiency of 40 % at 1330 K and 0.1 $s^{-1}$. Flow instabilities are observed in the material when the strain rates exceed roughly 3 $s^{-1}$ and temperatures range from 1260 to 1373 K. Furthermore, a small instability region appears at strain rates over 10 $s^{-1}$ and within the 1223–1230 K temperature range, resulting in flow localization. Up to a strain of 0.2, the MnCr-Si-V steel alloy map (Fig. 9 (a)) reveals two distinct domains: (1) The first domain of DRV occurs at temperatures between 1223 and 1373 K and strain rates from 0.01 to 1.5 $s^{-1}$, peaking at 37 % efficiency at 1335 K and 0.01 $s^{-1}$. (2) The second domain of DRX is found in the temperature range of 1298 to 1373 K and strain rates of 0.01 to 0.02 $s^{-1}$, achieving maximum efficiency of 44 % at 1373 K and 0.01 $s^{-1}$. Flow instabilities occur in the material at strain rates exceeding 10 $s^{-1}$ and temperatures between 1223 and 1228 K.

The instability regions for the MnCr-V steel alloy are found at strains of 0.2, 0.4, and 0.6 within the temperature ranges of 1265–1355 K, 1260–1373 K, and 1248–1373 K, respectively. Conversely, the instability regions of the MnCr-Si-V steel alloy at the same strains fall within the temperature ranges of 1223–1228 K, 1260–1373 K, and 1223–1373 K. Unlike the MnCr-V steel alloy, the MnCr-Si-V alloy exhibits an overlap between DRX and DRV.

Figs. 7 and 9 show that low-Si MnCr steel has superior dissipation efficiency and fewer instability zones, implying higher flow resistance during deformation. However, this enhanced resistance requires greater stress, which leads to increased energy consumption and equipment wear. Conversely, high-Si MnCr steel exhibits lower dissipation efficiency, fewer stable areas, and a heightened risk of instability, indicating reduced flow resistance, enhanced ductility, and better deformability, resulting in lower energy and force requirements during processing. Thus, MnCr-Si-V steel is the best option for hot deformation applications.

For both alloys, the safe processing domains, primarily associated with DRV and DRX, were identified in regions with moderate strain rates and higher temperatures. For instance, at a true strain of 0.6, the MnCr-V steel displayed stable DRX behavior in the temperature range of 1298–1373 K and strain rate range of 0.1–1 $s^{-1}$, while DRV occurred between 1223–1273 K and 0.01–0.03 $s^{-1}$. Similarly, for the MnCr-Si-V steel, DRX and DRV zones overlapped more broadly, with DRX occurring in 1260–1373 K and 0.03–1 $s^{-1}$, and DRV spanning a wider temperature and strain rate window. In contrast, instability zones, indicated by the red-shaded regions in the maps (Figs. 7 and 9), appeared predominantly at high strain rates (>3 $s^{-1}$) and low to intermediate temperatures, where adiabatic shear bands, flow localization, and potential wedge cracking at grain boundaries are likely. These regimes are therefore considered unsafe for industrial forming, especially under rapid or uncontrolled deformation conditions.

From an industrial perspective, the maps clearly demonstrate that MnCr-Si-V steel offers improved hot workability due to lower flow resistance, reduced energy requirements, and enhanced ductility, despite having slightly narrower stability regions. In contrast, although MnCr-V steel exhibits higher dissipation efficiency and broader safe zones, it requires higher stresses, which can increase tool wear and energy consumption during processing. Thus, the MnCr-Si-V steel is better suited for hot-forming applications where reduced force, enhanced ductility, and energy efficiency are desired.

### 3.6. *Microstructural evolution during annealing of the cold-rolled steels*

The heavily cold-rolled materials, with a 60 % reduction in thickness, underwent a brief 3-min annealing treatment at temperatures ranging from 800 to 1200 °C to promote the formation of new fine-grained structures. Following heavy cold-rolled deformation, the grain structures of the annealed steels were analyzed using LSCM, with examples presented in Figs. 10 and 11. At low annealing temperatures of 800 °C, minimal changes in the cold-rolled microstructure of MnCr-V steel were observed (not shown). This is mainly due to the low temperature and the precipitation of V(C,N) particles, which hindered static recrystallization (SRX). These particles successfully anchor the grain boundaries, thereby postponing SRX. This occurrence is characteristic of MnCr-V-N steels [80]. Scott et al. [81,82] studied the effects of V microalloying in high-Mn TWIP steels, where cold-rolled strips were annealed at 850 °C for 2 min to achieve optimal mechanical properties through precipitation strengthening. When annealed at a higher temperature of 900 °C, the microstructure showed partial recrystallization with fine recrystallized grains alongside flattened deformed original grains, as illustrated in Fig. 10(a). The structure exhibits some unusual characteristics, including long macroscopic shear bands indicated by black arrows and a tendency towards abnormal grain growth (Fig. 10(b)).

Following annealing at 1000 °C, a fully recrystallized ultra-fine structure was achieved, illustrated in Fig. 10(c). The structure shows an average grain size of 2 μm under higher magnification, as depicted in Fig. 10(d). However, a few larger equiaxed grains (highlighted by yellow circles) were observed. This suggests that the micron-sized grains were pinned by V(C,N) precipitates, but the pinning effect is lost locally, allowing grain growth. Allam et al. [6] conducted a thorough analysis of the precipitate structure in MnCr-V steel after 180 s of annealing at 1000 °C. The study revealed the presence of MN-type precipitates, particularly Cr-rich V(N,C), with a considerable average size exceeding 200 nm, and Cr-rich VN, which has a notably smaller average size of about 20 nm. Fig. 10(e) shows that the microstructure develops into a uniform fine-grained austenitic structure with equiaxed grains at an annealing temperature of 1100 °C. In contrast, at a higher annealing temperature of 1200 °C, intense grain growth leads to the formation of a coarse-grained structure, as depicted in Fig. 10(f). This structure features numerous annealing twins within the coarse grains, exhibiting shades of grey due

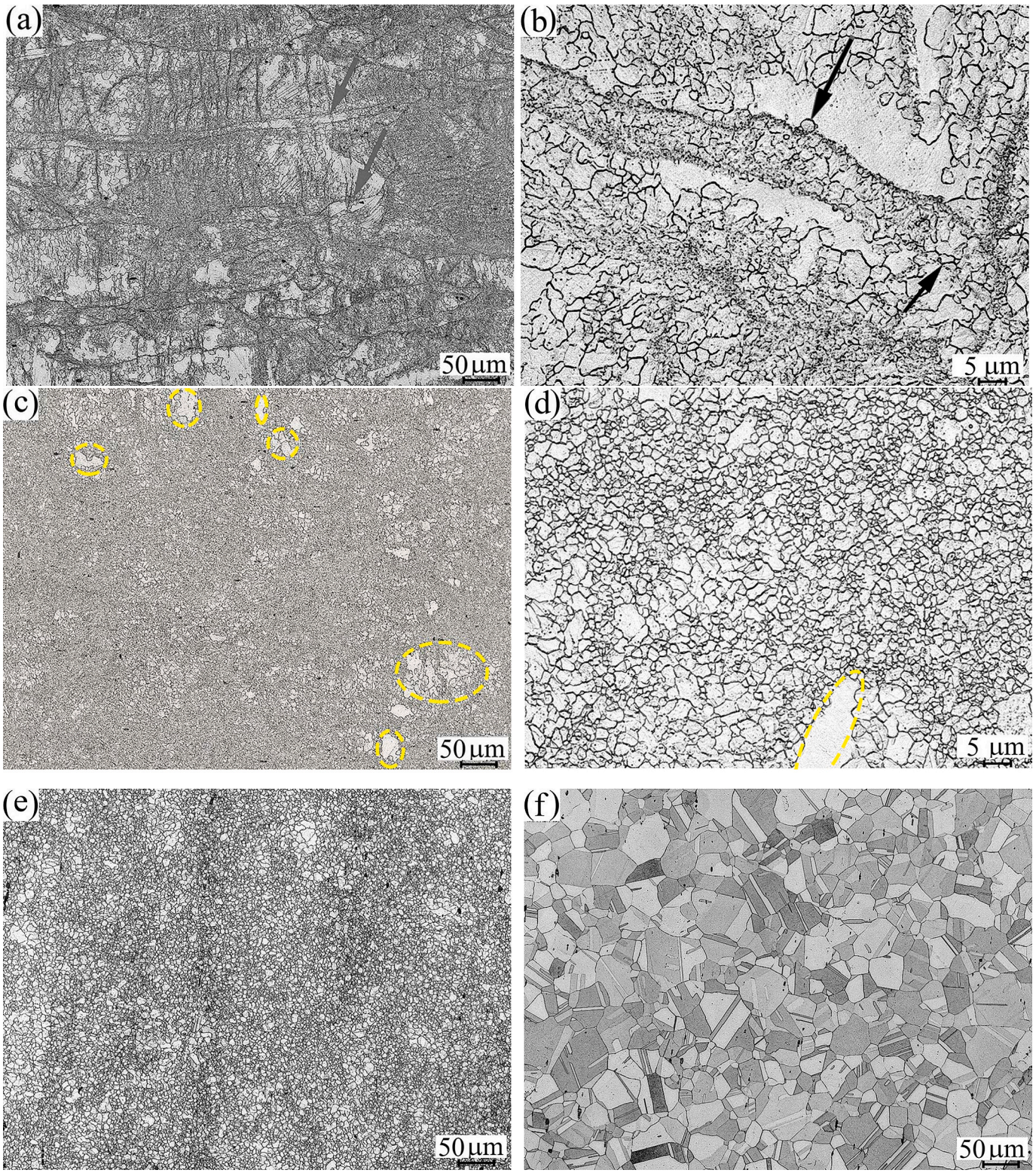


**Fig. 10.** Microstructures of MnCr-V steel annealed at different temperatures for 3 min: (a) 900 °C, (b) close-up of (a), (c) 1000 °C, (d) close-up of (c), (e) 1100 °C, and (f) 1200 °C. Images were captured with an LSCM.

to differing crystallographic orientations. These twins are typical in austenitic stainless steels and arise during the recrystallization and grain growth processes at elevated temperatures [83,84]. Annealing twins signify low SFE, which is estimated to be 34 mJ/m$^2$ at RT (see section 3.1).

The annealed microstructures of MnCr-Si-V steel show similarities and distinctions when compared to those of MnCr-V steel, as depicted in Fig. 11. At lower annealing temperatures (800–900 °C), the microstructure of MnCr-Si-V steel exhibits features of heavily deformed structures, akin to the MnCr-V steel, which include flattened, distorted grains and macroscopic shear bands marked by the red arrow in Fig. 11 (a). This indicates that significant recrystallization did not occur at these

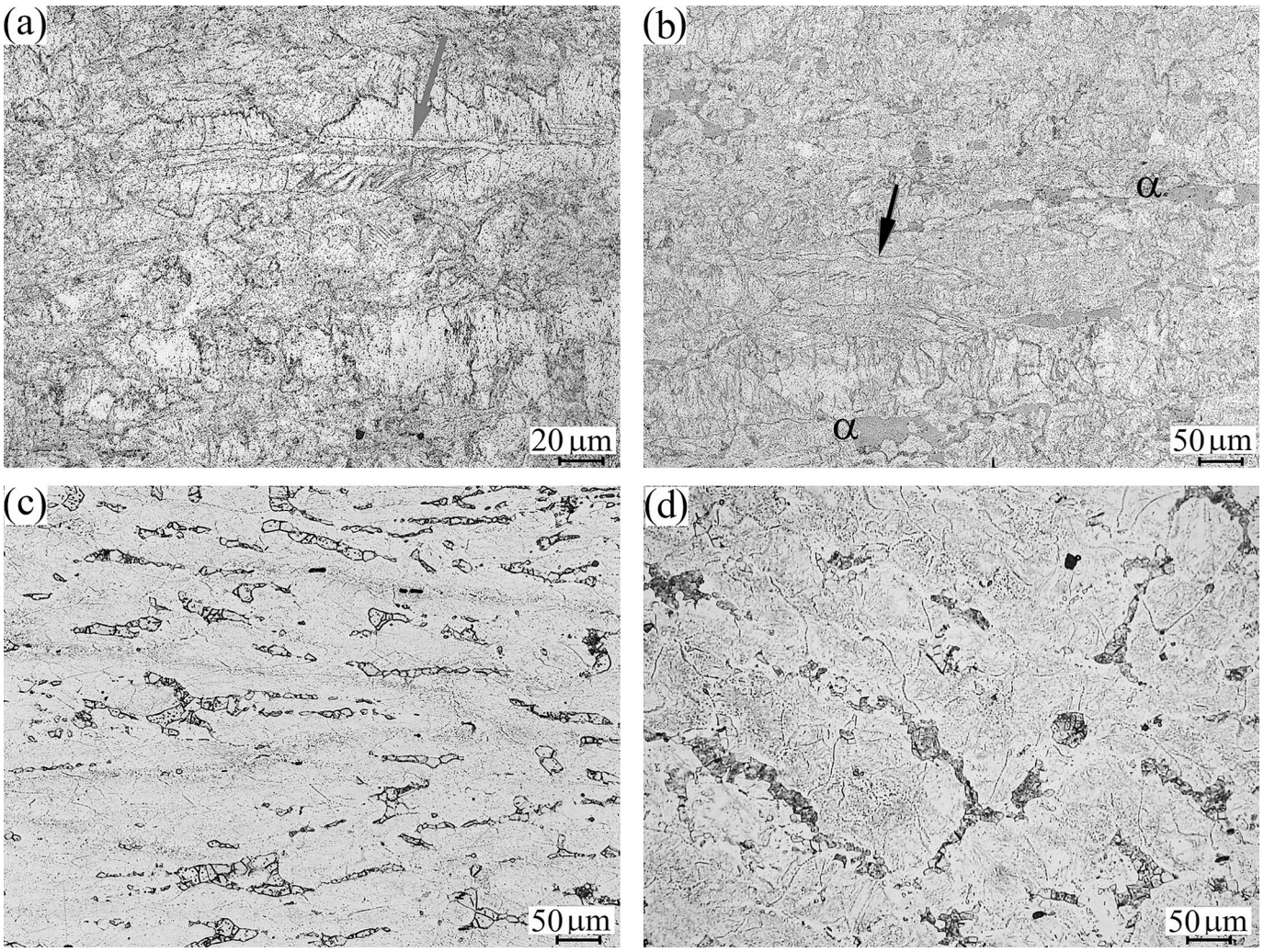


**Fig. 11.** Microstructures of the MnCr-Si-V steel subjected to annealing for 3 min at: (a) 900 °C, (b) 1000 °C, (c) 1100 °C, and (d) 1200 °C. The red arrows indicate distorted grains and extended shear bands. Images were captured using a LSCM.

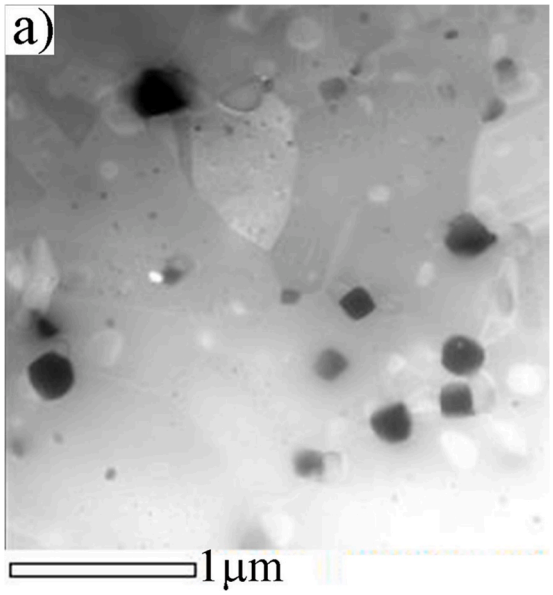


**Fig. 12.** STEM image and the corresponding elemental EDS maps of various types of precipitates in the annealed MnCr-Si-V at 1000 ∘C for 3 min after cold rolling. a) Bright-field image of the precipitates, and EDS elemental distribution maps for C, N, Cr, V, Mn, and Si.

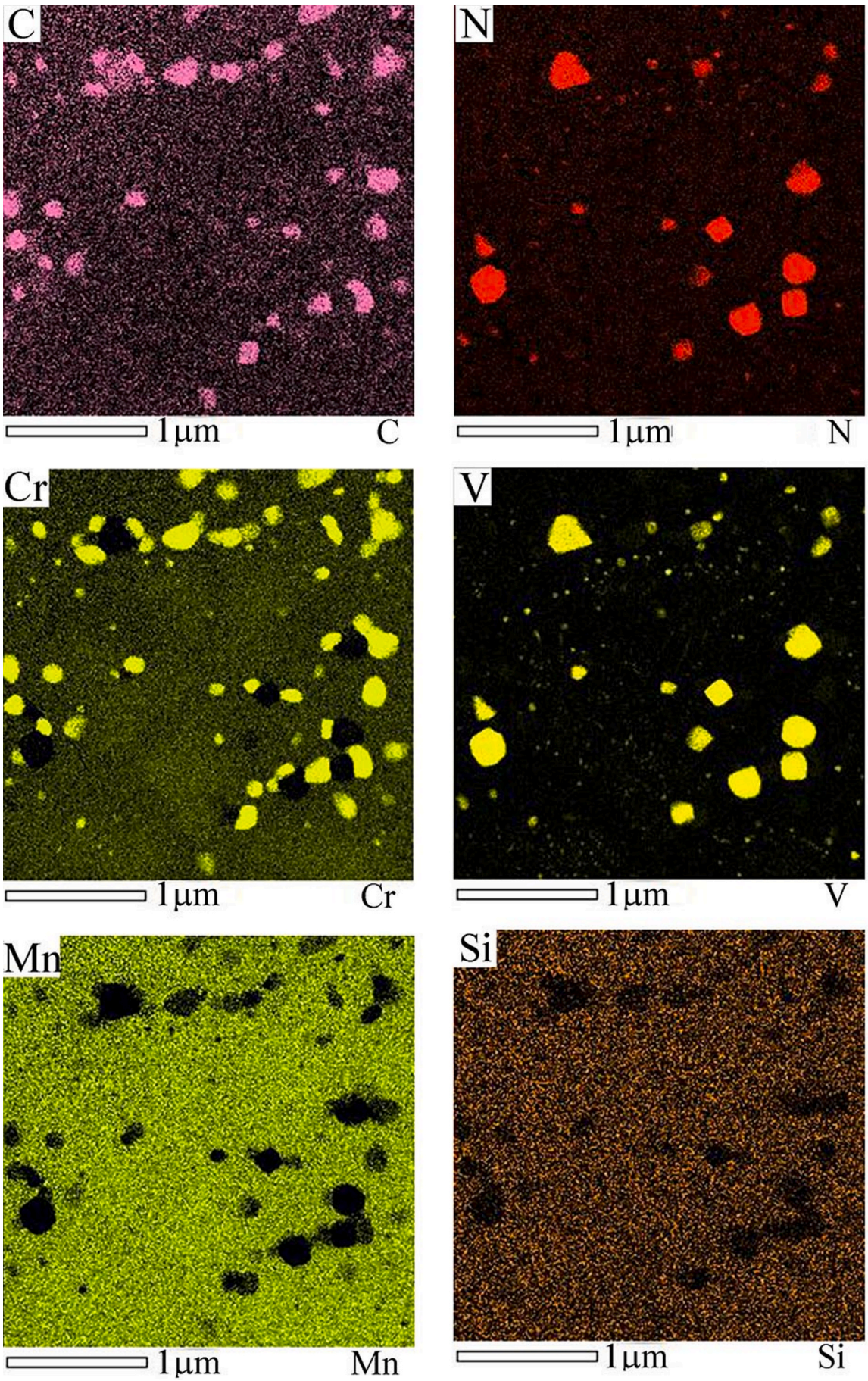


**Fig. 12.** (*continued*).

temperatures. In contrast, the MnCr-V steel annealed at 1000 °C displayed a fully recrystallized microstructure (Fig. 10(c, d)). Meanwhile, the microstructure of MnCr-Si-V steel continues to show clear signs of cold deformation, along with small dark grey areas indicating the ferrite phase, as seen in Fig. 11(b).

It is widely recognized that Si enhances the activity of C in austenite, stemming from the repulsive interaction between Si and C atoms [85]. This interaction increases the presence of both C and V in the matrix, aiding the creation of fine (VC) precipitates. As a result, Si is thought to indirectly encourage the nucleation of VC carbides, which serve as efficient barriers against softening due to SRX. This phenomenon is particularly noticeable in the partial SRX observed in the MnCr-Si-V steel at 1000 °C. Annealing at 1100 °C, the cold deformation microstructural features disappear, resulting in a duplex austenitic-ferritic structure, as shown in Fig. 11(c). According to the Thermo-Calc predictions outlined in Figs. S2 and S3, supported by Ref. [86], the ferrite phase is thermodynamically stable at temperatures ≥ 1030 °C in the MnCr-Si-V steel. In contrast, this stability threshold increases to 1240 °C for MnCr−V steel. The difference in the stability of ferrite is attributed to the effects of Si alloying, which lowers the stability temperature in these steels. It is worth noting that traces of ferrite were already observed during annealing at 1000 °C (Fig. 11(b)), but the alignment with the predicted lowest stability temperature of 1000 °C is fair. Ferrite was also seen after compression at 1000 °C (Fig. 4), but it might be retained ferrite from the earlier annealing at 1200 °C. The varying stability temperature of the ferrite phase in these steels accounts for the fact that the MnCr-V steel, when annealed at either 1100 °C or 1200 °C, did not show any ferrite phase (Fig. 10(e) and (f)). In contrast, Fig. 11(d) illustrates that the microstructure of the MnCr-Si-V steel annealed at 1200 °C features a duplex phase structure and larger grains.

Fig. 12 showcases a typical STEM image of the precipitates formed in MnCr-Si-V steel post-annealing at 1000 °C, and comprehensive elemental maps underscore their composition and distribution. The analysis identifies three unique precipitate types based on size and composition. The larger precipitates mainly consist of V(N) and V,Cr(N, C), whereas the intermediate-sized precipitates are primarily made up of Cr(C) and V,Cr(N). The finer precipitates mainly consist of V(N), as shown in the elemental distribution maps for V and N. This underscores the key roles of V, Cr, and N in forming and developing these precipitates. Further details regarding the characteristics and size distribution of the precipitates can be found in our manuscript [87].

A distinct characteristic of these precipitates is the absence of Mn and Si, as verified by their respective elemental maps. This suggests that Mn and Si primarily remain in the matrix and do not play a significant role in forming these precipitates. This conforms with their function of strengthening the matrix through solid solution hardening rather than carbide or nitride precipitation.

### 3.7. RT mechanical properties

Tensile tests were conducted at RT on cold-rolled specimens annealed for 3 min at various temperatures. The engineering stress–strain curves for MnCr-V and MnCr-Si-V steels are presented in Fig. 13, revealing comparable tensile behaviors across the annealing temperature range. The engineering flow curves display evident strain-hardening characteristics. The high-Si steel shows greater strength but less elongation than the low-Si steel. As annealing temperatures increase, the microstructure transitions from partially recrystallized, featuring fine grains, to fully recrystallized with more prominent grains and annealing twins, particularly at 1200 °C. This grain coarsening reduces strength but significantly enhances ductility, as illustrated in Fig. 13. The key mechanical properties, such as yield strength (YS), UTS, and total elongation (TE), were derived from the stress–strain curves and are presented in Table 5 and illustrated in Fig. 14. The fracture toughness, represented by the product of UTS and TE, is also summarized in Table 5.

After annealing at 800 °C, both types of steel exhibited impressive tensile strengths exceeding 1300 MPa; however, they also demonstrated significantly low ductility, with TE ranging from 6 % to 10 %. This characteristic is associated with the microstructure's retention of features from cold deformation. In contrast, annealing at 900 °C improved the elongation of the Mn-Cr-V steel, while the Mn-Cr-Si-V steel continued to exhibit low ductility. The specimen fractured suddenly without necking, achieving only 14 % elongation, which corresponds to a partially recrystallized structure. At 1000 °C, complete SRX occurred in the Mn-Cr-V steel, but only partial SRX was observed in the Mn-Cr-Si-V steel, evident in the higher elongation of the former steel. Coarse-grained structures obtained through annealing at 1200 °C resulted in an elongation of about 50 % in both types of steel.

The data presented in Table 5 indicate that the higher Si steel consistently shows higher YS and UTS values when compared to low-Si steel. This observation is consistent with earlier work by Jeong et al.

**Table 5**
Mechanical properties extracted from the tensile flow curves of the studied steels.

| T, °C | YS, MPa | | UTS, MPa | | TE, % | | UTS x TE, GPa% | |
|---|---|---|---|---|---|---|---|---|
| | 0.4Si- | 2Si-steel | 0.4Si- | 2Si-steel | 0.4Si- | 2Si-steel | 0.4Si- | 2Si-steel |
| 800 | 1164 | 1197 | 1320 | 1367 | 11 | 6 | 14.52 | 8.20 |
| 900 | 820 | 930 | 1064 | 1144 | 24 | 14 | 25.54 | 16.02 |
| 1000 | 665 | 715 | 980 | 1045 | 38 | 27 | 37.24 | 28.22 |
| 1100 | 494 | 510 | 905 | 944 | 43 | 38 | 38.92 | 35.87 |
| 1200 | 391 | 441 | 807 | 880 | 53 | 52 | 42.77 | 45.76 |

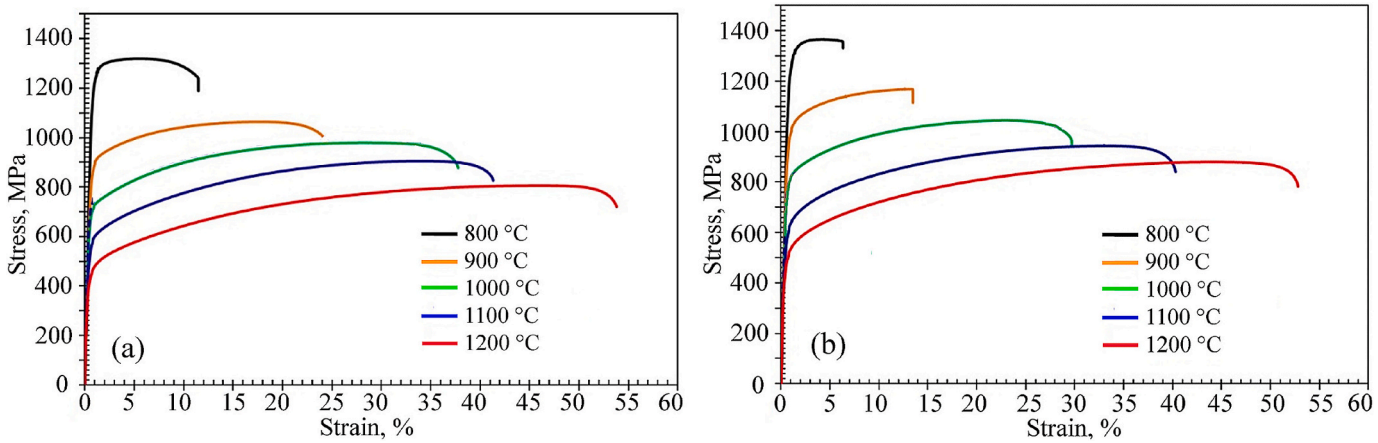


**Fig. 13.** Typical engineering stress–strain curves of the studied steels annealed at various temperatures for 3 min: (a) MnCr-V steel, and (b) MnCr-Si-V steel.

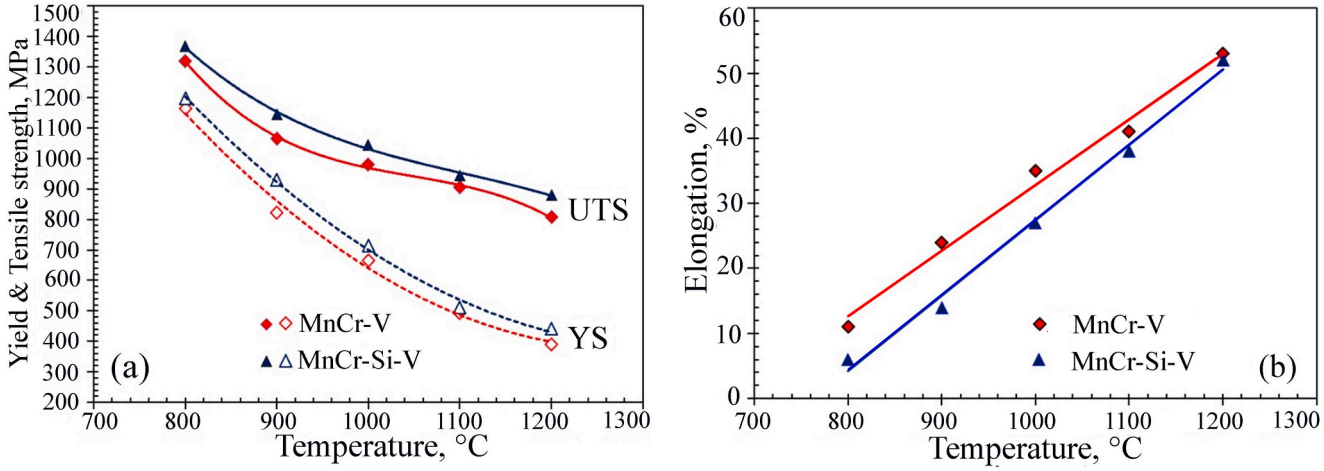


**Fig. 14.** Variation in YS and UTS as a function of prior annealing temperature for the MnCr-V and MnCr-Si-V steels, highlighting the influence of Si content on tensile properties. (a) YS and UTS and (b) TE . *(*MnCr-V *steel in red and* MnCr-Si-V*steel in blue).*

[46], who reported that the addition of 1.6 wt.% Si to a Fe-18Mn-0.6C steel increased YS by approximately 70 MPa. Li et al. [29] reported that incorporating 3 wt.% Si into 25Mn3Al steel, the YS increases from 200 MPa to 275 MPa, and the UTS from 475 MPa to 680 MPa. In this study, the distinctions in the YS between the studied steel are small, about 16 MPa and 50 MPa, after annealing at 1100 °C and 1200 °C, respectively. The distinctions in the counterparts' UTS values are 39 MPa and 73 MPa, respectively. The enhanced YS in higher Si steel is primarily due to solid solution hardening attributed to Si [46,88], and the presence of a small fraction of the ferrite phase, which is known to increase the UTS of Fe-Mn-based alloys at RT [57]. However, the strength values between the steels show their most significant difference following annealing at 900 °C, with YS at 110 MPa and UTS at 80 MPa. This highlights the substantial influence of cold deformation and the degree of SRX.

Table 5 indicates that the UTS × TE product values range from 15 to 43 GPa% for low (0.4Si) steel and 8 to 46 GPa% for high (2.2Si) steel. A significant increase is observed after annealing at 1000 °C for the lower Si steel and at 1100 °C for the higher Si steel, which is associated with SRX. This broad range suggests that the annealing temperature can be chosen to achieve a desirable combination of strength and ductility. The values of 35–45 GPa% can be considered reasonable.

To further characterize the tensile behavior of the studied steels, the true stress–strain curves were fitted using the power-law equation:

$$\sigma = K\varepsilon^{n} \tag{11}$$

In this context, σ represents the true stress, $K$ signifies the strength coefficient, ε denotes true plastic strain, and $n$ indicates the strain hardening exponent. Table 6 presents the extracted $K$ and $n$ parameters for both steels that were annealed at various temperatures. The findings reveal that the $n$-values increase with higher annealing temperatures, which aligns with the gradual development of SRX and grain coarsening. Interestingly, the high-Si steel tends to show slightly lower $n$-values at intermediate temperatures, particularly between 900–1000 °C, reflecting its partially recrystallized microstructure and limited ductility within this range. The $K$-values also consistently remain high across the temperature spectrum, demonstrating the steels' sustained work-hardening ability, especially following partial recovery and substructure preservation. This analysis enhances the tensile test results and provides a further understanding of the steels' strain hardening behavior and microstructural changes.

**Table 6**
$K$ and $n$ values obtained for both steels at various temperatures.

| Annealing Temp. | 0.4Si-(MnCr-V) | | 2Si-steel (MnCr-Si-V) | |
|---|---|---|---|---|
| | $K$ (MPa) | $n$ | $K$ (MPa) | $n$ |
| 800 °C | 1671 | 0.0624 | 1601 | 0.063 |
| 900 °C | 1555 | 0.1255 | 1716 | 0.1092 |
| 1000 °C | 1595 | 0.1888 | 1618 | 0.1596 |
| 1100 °C | 1545 | 0.2295 | 1594 | 0.2181 |
| 1200 °C | 1454 | 0.2747 | 1575 | 0.2647 |

Although a small amount of δ-ferrite can be beneficial during hot deformation by reducing flow stress, its presence at RT is generally undesirable in austenitic steels due to potential adverse effects on ductility and corrosion resistance. To mitigate this, post-deformation heat treatment strategies can be applied to suppress retained δ-ferrite. One such approach is solution annealing at temperatures slightly below the δ-ferrite stability threshold (~1030 °C), which facilitates the dissolution of δ-ferrite into the austenitic matrix while avoiding its reformation. This should be followed by controlled, slower cooling, which supports the completion of the diffusion-driven δ-ferrite-to-austenite transformation. Together, these treatments can reduce or eliminate δ-ferrite at RT, thereby improving the structural and corrosion performance of the high-Si steel.

The addition of Si to MnCr-V austenitic steels presents a balance of benefits and trade-offs. On the one hand, Si enhances solid-solution strengthening, increases carbon activity (promoting V(C,N) precipitation), and slightly raises the SFE, all of which contribute to higher yield and tensile strength. Moreover, Si promotes the formation and stabilization of δ-ferrite at high temperatures, which can be advantageous during hot deformation by reducing flow stress and improving processability. On the other hand, retaining δ-ferrite at RT may negatively affect ductility and corrosion resistance. Therefore, optimizing the Si content necessitates careful control of thermomechanical processing parameters and post-deformation heat treatments to utilize its strengthening and processing advantages while minimizing the adverse effects of retained δ-ferrite. This study emphasizes the significance of managing this trade-off to achieve a favorable balance of strength, ductility, and formability in high-performance stainless steel.

Si indirectly promotes the nucleation of V(C,N) precipitates by enhancing the carbon activity in the matrix due to the repulsive interaction between Si and C atoms [85]. This effect increases the availability of both C and V in the matrix, facilitating the formation of fine V(C,N) precipitates during annealing. These V(C,N) precipitates serve as strong obstacles to dislocation motion and grain boundary migration, significantly contributing to precipitation strengthening and impeding softening mechanisms, particularly in partially recrystallized microstructures.

This precipitation-strengthening mechanism is particularly evident

in the MnCr-Si-V steel annealed at 900–1000 °C, where only partial SRX with a fine-grained structure was observed. The presence of finely dispersed V(C,N) precipitates likely impedes dislocation movement, resulting in a higher dislocation density and increased strength, despite limited ductility. This is reflected in the mechanical property data (Table 5), where the high-Si steel maintains UTS values of 1145 and 1045 MPa after annealing at 900 and 1000 °C, respectively. The corresponding UTS × TE products are 28.2 GPa% and 35.9 GPa%.

In addition to their strengthening role, the V(C,N) precipitates can influence deformation twinning in the surrounding matrix due to local stress concentration and interactions with stacking faults. This mechanism suggests that the V(C,N) precipitates may locally facilitate twinning, contributing to strain hardening and enhancing the strength–ductility synergy. Thus, the combined effects of solid solution strengthening from Si, precipitate strengthening from VC, and enhanced twinning through local stress fields help mitigate the loss of ductility typically associated with strengthening mechanisms alone. This synergy leads to favorable UTS × TE values (35–46 GPa%) in the high-Si steel, particularly following high-temperature annealing.

Aging at 800–900 °C for brief periods (about 180 s) enhances the effective precipitation of V(C,N), utilizing as much as 70 % of the available vanadium and nitrogen solutes. This quick precipitation process at moderate temperatures results in a high density of fine precipitates, which greatly aids in strengthening while avoiding significant coarsening.

The mechanical properties outlined in Section 3.7, Table 6, show a distinct trend in the strength coefficient (K). It increases from 800 to 900 °C before gradually decreasing at higher annealing temperatures. This observation emphasizes the impact of aging temperature on the strengthening mechanism due to the precipitation hardening. Scott et al. [81] discovered that brief aging at intermediate temperatures (800–900 °C) for approximately 180 s leads to the most efficient precipitation of V(C,N), utilizing around 70 % of the available V and N solutes. These conditions promote a dense distribution of fine precipitates that strongly impede dislocation motion, enhancing strength. The high K values for both steels at 800–900 °C observed in Table 6 are attributed to this precipitation strengthening effect. Above this temperature range, precipitate coarsening and increased recrystallization reduce strengthening contributions, leading to lower K values. Therefore, the precipitation strengthening effect of VN and V(C,N) precipitates in this optimal temperature range significantly contributes to the observed strength peak, particularly in the high-Si steel.

### 3.8. Strengthening mechanisms

The yield strengths of the two alloys after treatment at various temperatures can be considered the sum of three strengthening mechanisms: solid solution strengthening, strengthening due to dislocation/precipitate interactions, and grain size strengthening [89]:

$$\sigma_y = \Delta\sigma_{ss} + \Delta\sigma_{ps} + \Delta\sigma_{gs} \tag{12}$$

The contributions of the three mechanisms mentioned above are evaluated as follows.

#### 3.8.1. Solid solution strengthening

The strengthening effect of solute atoms has been modeled by Labusch [90] and subsequently modified by Nabarro [91]. The Labusch-Nabarro equation, presented below, is commonly used to quantify the contribution of solute atoms to solid solution hardening:

$$\Delta\tau_{L-N} = \frac{\left(2\omega f_m^4 c^2\right)^{1/3}}{2b^{7/3}\left(Gb^2\right)^{1/3}} \tag{13}$$

Where $f_m$ is the maximum interaction force between the solute atom and the matrix (solvent), $\omega$ is an adjusting parameter for the interaction force, c is the atomic percent of each solute atom in the alloy, b is the magnitude of the Burgers vector, and G is the shearing modulus of elasticity. The maximum interaction force, $f_m$, depends on the lattice strain induced due to the size misfit between the solute and solvent atoms ($\varepsilon_s$)[92]:

$$f_m = \alpha\varepsilon_s G b^2/120 \tag{14}$$

Where $\alpha$ is a constant usually in the range 9–16 [93]. The solute/solvent size misfit ($\varepsilon_s$) is defined based on the gradient of Burgers vector magnitude with the concentration of the solute atom:

$$\varepsilon_s = \frac{1}{b}\frac{db}{dc} \tag{15}$$

The atomic volume of FCC crystals is related to their Burgers in the form: $V = b^3/\sqrt{2}$. On the other hand, Vegard's law [94] suggests that atomic volumes of the solute and solvent obey the following equation when they are mixed:

$$\frac{dV}{dc} = V_1 - V_2 \tag{16}$$

Where $V_1$ and $V_2$ are the atomic volumes of the solvent and the solute, respectively. By applying the chain rule to the above derivatives, it can be seen that:

$$\frac{db}{dc} = \frac{V_1 - V_2}{3b^2/\sqrt{2}} \tag{17}$$

Thus, by inserting Eqs. (14), 15 and 17 into Eq. (13) and utilizing the Taylor factor (m) for FCC systems, the solid solution strengthening ($\Delta\sigma$) of each individual solute element can be estimated. The results of this calculation for the present steels, as well as the model parameters, are presented in Table 7. The contribution of solid solution strengthening ($\Delta\sigma_{ss}$) can be simply calculated by summing up the influences of the alloying elements [93].

#### 3.8.2. Strengthening due to precipitates

The influence of precipitates on the strengthening of the alloy is modeled using the well-known equation of Orowan-Ashby [95]:

$$\Delta\sigma_{ps} = \frac{0.13Gb}{\lambda}\ln\left(\frac{r}{b}\right) \tag{18}$$

Where $\lambda$ is the average distance between the precipitates and r is the average radius of the precipitates. These two parameters are determined based on the interpretation previously conducted in [6] which gives approximate values of ~ 10 and 100 nm for r and $\lambda$, respectively. Based on these values, a strengthening as large as 91 MPa is calculated as the contribution of the precipitates.

**Table 7**
Labusch-Nabarro model parameters and the strengthening contributions of the alloying elements.

| Parameter, unit | value | Parameter | value |
|---|---|---|---|
| m | 3.06 | $\varepsilon_{s,Cr}$ | 0.006837 |
| $\alpha$ | 9 | $\varepsilon_{s,Mn}$ | 0.026243 |
| b, meter | $2.5 \times 10^{-10}$ | $\varepsilon_{s,Ni}$ | 0.025081 |
| $\omega$ | 5 × b [93] | $\varepsilon_{s,Si}$ | 0.248282 |
| G, MPa | 76,000 | $\varepsilon_{s,V}$ | 0.062188 |
| 0.4Si- (MnCr-V) steel | | | |
| $\Delta\sigma_{Cr}$, MPa | 3 | $\Delta\sigma_{Si}$, MPa | 52 |
| $\Delta\sigma_{Mn}$, MPa | 14 | $\Delta\sigma_{V}$, MPa | 10 |
| $\Delta\sigma_{Ni}$, MPa | 7 | $\Delta\sigma_{ss}$, MPa | 86 |
| 2Si- (MnCr-Si-V) steel | | | |
| $\Delta\sigma_{Cr}$, MPa | 3 | $\Delta\sigma_{Si}$, MPa | 155 |
| $\Delta\sigma_{Mn}$, MPa | 14 | $\Delta\sigma_{V}$, MPa | 9 |
| $\Delta\sigma_{Ni}$, MPa | 7 | $\Delta\sigma_{ss}$, MPa | 189 |

### 3.8.3. The influence of grain sizes

The grain size strengthening is considered here via the classical Hall-Petch equation:

$$\Delta\sigma_{gs} = \sigma_0 + kd^{-1/2} \tag{19}$$

Where $\sigma_0$ is the lattice friction stress, k is a constant and d is the average grain diameter. The first two are determined here by fitting. The parameters of Hall-Petch equation are presented in Table 8.

**Table 8**
The Hall-Petch equation parameters and data used in modeling the grain size strengthening contribution.

| Parameter | Value |
|---|---|
| 0.4Si- (MnCr-V) steel | |
| $\sigma_0(MPa)$ | 184.31 |
| K $(MPa.\sqrt{\mu m})$ | 285.39 |
| 2Si- (MnCr-Si-V) steel | |
| $\sigma_0(MPa)$ | 111.35 |
| K $(MPa.\sqrt{\mu m})$ | 303.19 |
| Grain size data | |
| Annealing temperature (°C) | Average grain size $(\mu m)$ |
| 800 | 0.2 |
| 900 | 0.2 |
| 1000 | 1.2 |
| 1100 | 4 |
| 1200 | 34 |

**Table 9**
The contribution of different strengthening mechanisms to the yield strengths of various experimental materials.

| 0.4Si- (MnCr-V) steel<br>Annealing temperature (°C) | $\sigma_y$(MPa) | $\sigma_{ss}$(MPa) | $\sigma_{ps}$(MPa) | $\sigma_{gs}$(MPa) |
|---|---|---|---|---|
| 800 | 1164 | 86 | 91 | 987 |
| 900 | 821 | | | 644 |
| 1000 | 665 | | | 488 |
| 1100 | 494 | | | 317 |
| 1200 | 391 | | | 214 |
| 2Si- (MnCr-Si-V) steel | | | | |
| Annealing temperature (°C) | $\sigma_y$(MPa) | $\sigma_{ss}$(MPa) | $\sigma_{ps}$(MPa) | $\sigma_{gs}$(MPa) |
| 800 | 1197 | 189 | 91 | 917 |
| 900 | 930 | | | 650 |
| 1000 | 715 | | | 435 |
| 1100 | 510 | | | 230 |
| 1200 | 441 | | | 161 |

Based on the three strengthening models discussed above, the contribution of each mechanism to the yield strength of the studied steels can be summarized in Table 9. Expectedly, the contribution of the Hall-Petch mechanism considerably increases with decreased grain size.

### 3.9. Microstructures after tensile tests

The microstructures of MnCr-V and MnCr-Si-V steels were analyzed after a 3-minute high-temperature annealing process (1100–1200 °C), followed by tensile testing at RT.

In Fig. 15(a), the IQ map shows flattened grains aligned with the tensile axis, featuring distinct black lines representing slip bands and mechanical twins. The orientation map in Fig. 15(b) reveals local differences in grain orientation, highlighted by various colors within individual grains, like Grain A. A significant deformation band intersects grain **A**.

The boundary map in Fig. 15(c) distinguishes between slip bands and mechanical twins. Slip bands show no orientation variations from the matrix, while Σ3 boundaries indicate the presence of twins. The map displays a notable concentration of Σ3 boundaries, highlighted in red, with a fraction of 0.42, underscoring the active TWIP effect during tensile deformation. This demonstrates that the desired TWIP deformation mode in the steel was achieved by adjusting the SFE to about 34 $mJ/m^2$.

Similarly, the microstructure of MnCr-Si-V steel, which was annealed at 1100 °C and then strained to failure at RT, exhibited comparable deformation characteristics. Fig. 16(a) shows that the deformed grain structure appears darker grey in the IQ map, indicating a high intrinsic dislocation density within these grains. Previous studies have documented the correlation between greyscale intensity, dislocation density, and phase type [96]. Darker grey shades indicate that the microstructure underwent significant deformation, leading to a high dislocation density and visible slip lines.

The corresponding orientation map in Fig. 16(b) shows that the tensile-strained grains have ⟨101⟩ (green) and ⟨111⟩ (blue) crystallographic orientations. Meanwhile, the boundary map in Fig. 16(c) highlights the critical role of the TWIP mechanism in tensile deformation. This is supported by a high fraction (around 0.38) of Σ3 boundaries, typical of mechanical twins. However, this value is slightly lower than the 0.42 observed in MnCr-V steel, indicating somewhat reduced twinning activity in MnCr-Si-V steel.

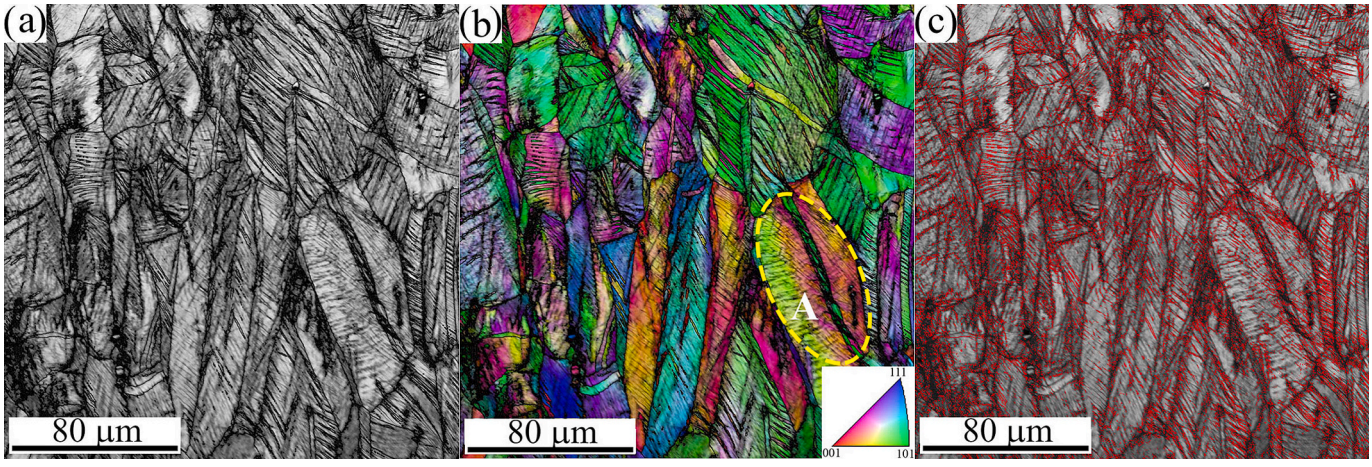


**Fig. 15.** EBSD maps of cold-rolled MnCr-V steel annealed at 1200 °C and tensile strained until failure: (a) IQ map, (b) IPF map of (a), and (c) boundary map highlighting mechanical twins in red.

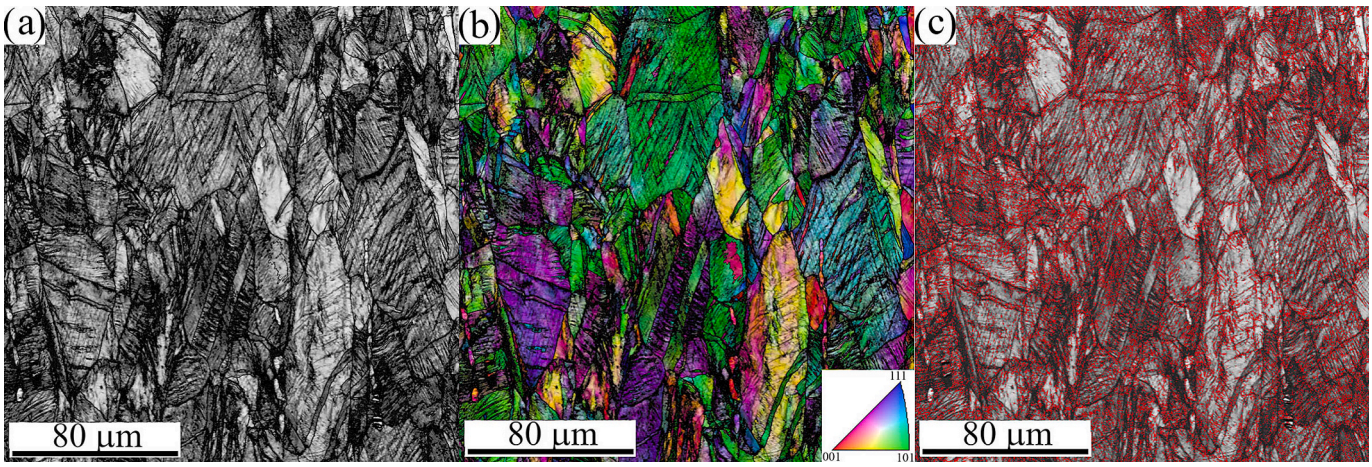


**Fig. 16.** EBSD maps of MnCr-Si-V steel annealed at 1100 °C and tensile strained until failure: (a) IQ map, (b) IPF map of (a), and (c) boundary map highlighting mechanical twins in red.

## 4. Conclusions

Two variants of V-microalloyed MnCr stainless steels (Fe-0.17C-10Mn-18Cr-5Ni-1V-0.25N-xSi) were produced, with Si contents of 0.4 and 2.2 wt.%. These steels demonstrate the distinct effects of Si in two key aspects: 1) high-temperature deformation evaluated through compression tests conducted between 950 and 1100 °C, and 2) mechanical strength assessed via tensile tests at RT after rapid annealing of heavily cold-rolled steel sheets at temperatures from 900 to 1200 °C for 3 min. The main findings from this research are summarized below:

(1) The MnCr-V steel with low Si (0.4 wt.%) maintained a fully austenitic microstructure after hot rolling. In contrast, adding 2.2 wt.% Si resulted in a stable duplex microstructure comprised of austenite and 7 % ferrite.
(2) The MnCr-V steel with low Si demonstrated higher flow stress during hot deformation than the MnCr-Si-V steel with high Si. This difference was particularly noticeable at temperatures between 950 and 1000 °C and at low strain rates (approximately 0.1 $s^{-1}$). The increased flow stress is associated with enhanced DRX due to Si alloying and the soft ferrite phase resulting from prior annealing at 1200 °C.
(3) The activation energy of hot deformation decreased markedly from 507 kJ/mol to 447 kJ/mol upon adding 2.2 wt.% Si. This change results from the ferrite phase in the MnCr-Si-V steel, which possesses significantly lower activation energy for deformation.
(4) The processing maps clearly illustrate that MnCr-V steel has superior dissipation efficiency and stability; however, it requires more energy and increases equipment wear. Conversely, MnCr-Si-V steel offers improved deformability and lower energy requirements, but it is less stable, making it the preferred choice for hot deformation processes.
(5) The formation of V(C,N) particles at 800 °C impeded softening during 3-min FH annealing of cold-rolled steels. As the annealing temperature increased, the microstructure changed from partially recrystallized at 900 °C to ultrafine-grained at 1000 and 1100 °C, ultimately leading to a coarse-grained structure at 1200 °C. The SRX process was completed within 3 min at 1000 °C in Mn-Cr-V steel, remaining only partial at 1100 °C in Mn-Cr-Si-V steel.
(6) Si alloying enhanced mechanical strength, YS and UTS, at RT following cold rolling and annealing. The most significant strength difference occurred after annealing at 900 °C, driven by variations in recrystallization levels. However, this increase in strength led to a decrease in tensile elongation. The peak UTS × TE product of 46 GPa% was achieved in the Mn-Cr-Si-V steel after 1200 °C annealing.
(7) In both types of steel, a significant TWIP effect was evident during tensile testing following cold rolling and FH annealing, as shown by the high concentration of mechanical twins and Σ3 twin boundaries in their microstructures. This phenomenon was more pronounced in the MnCr-V steel, which exhibited a slightly higher proportion of Σ3 boundaries (~0.42) than the MnCr-Si-V steel (~0.38).

## CRediT authorship contribution statement

**Atef Hamada:** Conceptualization, Investigation, Data curation, Formal analysis, Validation, Visualization, Writing – original draft, Writing – review & editing, Project administration. **Ali Khosravifard:** Software, Formal analysis. **Khaled Elanany:** Software, Formal analysis. **Mahmoud Khedr:** Writing – original draft. **Anna Kisko:** Methodology. **Matias Jaskari:** Methodology. **Saad Ebied:** Formal analysis. **Tarek Allam:** Review & editing.. **Antti Järvenpää:** Resources. **Pentti Karjalainen:** Writing – review & editing, Supervision.

## Declaration of competing interest

The authors declare that they have no known competing financial interests or personal relationships that could have appeared to influence the work reported in this paper.

## Acknowledgment

A. Hamada gratefully acknowledges the support of the Science and Technology Development Fund (STDF), The Egyptian Ministry of Higher Education and Scientific Research, Cairo, for funding this work through the National Challenges Program (Project No. STDF-NCP-10751). The authors also extend their gratitude to the Materials and Mechanical Engineering (MME) at the University of Oulu for providing technical support in conducting the rolling processes and hot deformation tests using the Gleeble simulator.

## Appendix A. Supplementary data

Supplementary data to this article can be found online at https://doi.org/10.1016/j.matdes.2025.114072.

## Data availability

The data that support the findings of this study are available from the corresponding author upon reasonable request.

## References


[1] B. Hu, H. Luo, F. Yang, H. Dong, Recent progress in medium-Mn steels made with new designing strategies, a review, J. Mater. Sci. Technol. 33 (2017) 1457–1464, https://doi.org/10.1016/j.jmst.2017.06.017.

[2] E. Doruk, S. Demir, New generation steels for light weight vehicle safety related applications, Mater, TEST 66 (2024) 992–998, https://doi.org/10.1515/MT-2024-0052/MACHINEREADABLECITATION/RIS.

[3] K. Jasiak, Z. Gronostajski, M.B. Jabłońska, Experimental and numerical determination of the temperature of TWIP steel during dynamic tensile testing, J. Mater. Res. Technol. 28 (2024) 856–864, https://doi.org/10.1016/J.JMRT.2023.12.056.

[4] F. De Barbieri, D. Jorge-Badiola, R. Allende, K. Tello, A. Artigas, F. Perazzo, H. Jami, J.P. Ipiña, Effect of Cr content in temperature-dependent mechanical properties and strain hardening of a twinning-induced plasticity steel, Mater. Sci. Eng. A. 889 (2024) 145865, https://doi.org/10.1016/J.MSEA.2023.145865.

[5] T.W.J. Kwok, D. Dye, A review of the processing, microstructure and property relationships in medium Mn steels, Int. Mater. Rev. 68 (2023) 1098–1134, https://doi.org/10.1080/09506608.2023.2199617.

[6] T. Allam, X. Guo, M. Lipinska-Chwalek, A. Hamada, E. Ahmed, W. Bleck, Impact of precipitates on the hydrogen embrittlement behavior of a V-alloyed medium-manganese austenitic stainless steel, J. Mater. Res. Technol. 9 (2020) 13524–13538, https://doi.org/10.1016/J.JMRT.2020.09.085.

[7] A.S. Hamada, L.P. Karjalainen, R.D.K. Misra, J. Talonen, Contribution of deformation mechanisms to strength and ductility in two Cr-Mn grade austenitic stainless steels, Mater. Sci. Eng. A. 559 (2013) 336–344, https://doi.org/10.1016/j.msea.2012.08.108.

[8] A.S. Hamada, L.P. Karjalainen, Hot ductility behaviour of high-Mn TWIP steels, Mater. Sci. Eng. A. 528 (2011) 1819–1827, https://doi.org/10.1016/J.MSEA.2010.11.030.

[9] S.E. Kang, M.H. Kang, B. Mintz, Influence of vanadium, boron and titanium on hot ductility of high Al, TWIP steels, Mater. Sci. Technol. (united Kingdom) 37 (2021) 42–58, https://doi.org/10.1080/02670836.2020.1861736.

[10] Introducing the TWIP strengthening mechanism | Outokumpu, (n.d.). https://www.outokumpu.com/expertise/2020/introducing-the-twip-strengthening-mechanism (accessed January 20, 2025).

[11] S. Curtze, V.T. Kuokkala, Dependence of tensile deformation behavior of TWIP steels on stacking fault energy, temperature and strain rate, Acta Mater. 58 (2010) 5129–5141, https://doi.org/10.1016/J.ACTAMAT.2010.05.049.

[12] M. Khedr, W. Li, N. Min, W. Liu, X. Jin, Effects of increasing the strain rate on mechanical twinning and dynamic strain aging in Fe-12.5Mn-1.1C and Fe–24Mn-0.45C–2Al austenitic steels, Mater. Sci. Eng. A. 842 (2022) 143024, https://doi.org/10.1016/J.MSEA.2022.143024.

[13] C. Wang, W. Cai, C. Sun, X. Li, L. Qian, J. Jiang, Strain rate effects on mechanical behavior and microstructure evolution with the sequential strains of TWIP steel, Mater. Sci. Eng. A. 835 (2022) 142673, https://doi.org/10.1016/J.MSEA.2022.142673.

[14] M. Khedr, W. Li, N. Min, W. Abd-Elaziem, X. Jin, Strengthening contributions of mechanical twinning and dislocations to the flow stress of hadfield high-manganese steel: quantitative analysis, J. Mater. Eng. Perform. 32 (2023) 501–511, https://doi.org/10.1007/S11665-022-07113-8/FIGURES/7.

[15] M.F. Sklate Boja, A.V. Druker, Controlling mechanical behavior of TWIP steels by tuning texture and stacking faults, Metall. Mater. Trans. A Phys. Metall. Mater. Sci. 53 (2022) 3986–4003, https://doi.org/10.1007/S11661-022-06804-0/FIGURES/17.

[16] H. Essoussi, S. Ettaqi, E. Essadiqi, On the prediction of stacking fault energy on medium Mn steels, Phys. Met. Metallogr. 122 (2021) 1507–1512, https://doi.org/10.1134/S0031918X21140076/FIGURES/7.

[17] Y.W. Choi, Z. Dong, W. Li, S. Schönecker, H. Kim, S.K. Kwon, L. Vitos, Predicting the stacking fault energy of austenitic Fe-Mn-Al (Si) alloys, Mater. Des. 187 (2020) 108392, https://doi.org/10.1016/J.MATDES.2019.108392.

[18] R. Xiong, Y. Liu, H. Si, H. Peng, S. Wang, B. Sun, H. Chen, H.S. Kim, Y. Wen, Effects of Si on the Microstructure and Work Hardening Behavior of Fe17Mn1.1CxSi High Manganese Steels, Met. Mater. Int. 27 (2021) 3891–3904, https://doi.org/10.1007/S12540-020-00846-Y/FIGURES/10.

[19] B. Mintz, A. Qaban, The Influence of Precipitation, High Levels of Al, Si, P and a Small B Addition on the Hot Ductility of TWIP and TRIP Assisted Steels: A Critical Review, Metals (basel). 12 (2022), https://doi.org/10.3390/met12030502.

[20] T. Chen, G. Li, H. Wang, X. An, X. Huang, Effect of Si content on the mechanical behavior and microstructure of a 9Cr ferritic/martensitic steel, J. Mater. Res. Technol. 29 (2024) 1542–1556, https://doi.org/10.1016/J.JMRT.2024.01.239.

[21] H. Gwon, J.K. Kim, S. Shin, L. Cho, B.C. De Cooman, The effect of vanadium micro-alloying on the microstructure and the tensile behavior of TWIP steel, Mater. Sci. Eng. A. 696 (2017) 416–428, https://doi.org/10.1016/J.MSEA.2017.04.083.

[22] Y. Li, Y. Lu, W. Li, M. Khedr, H. Liu, X. Jin, Hierarchical microstructure design of a bimodal grained twinning-induced plasticity steel with excellent cryogenic mechanical properties, Acta Mater. 158 (2018) 79–94, https://doi.org/10.1016/J.ACTAMAT.2018.06.019.

[23] N. Bi, H. Tang, Z. Shi, X. Wang, F. Han, J. Liang, Effects of Vanadium Microalloying and Intercritical Annealing on Yield Strength-Ductility Trade-Offs of Medium-Manganese Steels, Mater 16 (2023) 2220, https://doi.org/10.3390/MA16062220.

[24] A. Khosravifard, A.S. Hamada, M.M. Moshksar, R. Ebrahimi, D.A. Porter, L. P. Karjalainen, High temperature deformation behavior of two as-cast high-manganese TWIP steels, Mater. Sci. Eng. A. 582 (2013) 15–21, https://doi.org/10.1016/J.MSEA.2013.06.014.

[25] V. Torganchuk, O. Rybalchenko, S.V. Dobatkin, A. Belyakov, R. Kaibyshev, Hot deformation and dynamic recrystallization of 18%Mn twinning-induced plasticity steels, Adv. Eng. Mater. 22 (2020) 2000098, https://doi.org/10.1002/ADEM.202000098.

[26] H.N. Choi, J.W. Choi, H. Kang, H. Fujii, S.J. Lee, Effect of stacking-fault energy on dynamic recrystallization, textural evolution, and strengthening mechanism of Fe−Mn based twinning-induced plasticity (TWIP) steels during friction-stir welding, J. Adv. Join. Process. 10 (2024) 100236, https://doi.org/10.1016/J.JAJP.2024.100236.

[27] Z. Zhang, C. Song, W. Wu, H. Wang, Z. Sun, Investigating the influence of Si on dynamic recrystallization during hot deformation behavior of ultra-high-strength lightweight steel, J. Mater. Res. Technol. 27 (2023) 8084–8099, https://doi.org/10.1016/j.jmrt.2023.11.242.

[28] B.C. De Cooman, O. Kwon, K.G. Chin, State-of-the-knowledge on TWIP steel, Mater. Sci. Technol. 28 (2012) 513–527, https://doi.org/10.1179/1743284711Y.0000000095.

[29] D. Li, Y. Feng, S. Song, Q. Liu, Q. Bai, F. Ren, F. Shangguan, Influences of silicon on the work hardening behavior and hot deformation behavior of Fe–25 wt.%Mn–(Si, Al) TWIP steel, J. Alloys Compd. 618 (2015) 768–775, https://doi.org/10.1016/J.JALLCOM.2014.08.239.

[30] L. Li, H. Wu, C. Guo, Y. Feng, Deformation behavior and softening mechanism in ferrite steel during warm deformation, J. Mater. Res. Technol. 18 (2022) 3977–3990, https://doi.org/10.1016/J.JMRT.2022.04.067.

[31] H. Khatami-Hamedani, A. Zarei-Hanzaki, H.R. Abedi, A.S. Anoushe, L. P. Karjalainen, Dynamic restoration of the ferrite and austenite phases during hot compressive deformation of a lean duplex stainless steel, Mater. Sci. Eng. A. 788 (2020) 139400, https://doi.org/10.1016/J.MSEA.2020.139400.

[32] B.C. De Cooman, Y. Estrin, S.K. Kim, Twinning-induced plasticity (TWIP) steels, Acta Mater. 142 (2018) 283–362, https://doi.org/10.1016/J.ACTAMAT.2017.06.046.

[33] O. Bouaziz, S. Allain, C.P. Scott, P. Cugy, D. Barbier, High manganese austenitic twinning induced plasticity steels: A review of the microstructure properties relationships, Curr. Opin. Solid State Mater. Sci. 15 (2011) 141–168, https://doi.org/10.1016/J.COSSMS.2011.04.002.

[34] M.C. Somani, D.A. Porter, A.S. Hamada, L.P. Karjalainen, High-temperature flow stress and recrystallization characteristics of Al-bearing microalloyed TWIP steels, Metall. Mater. Trans. A Phys. Metall. Mater. Sci. 46 (2015) 5329–5342, https://doi.org/10.1007/S11661-015-3112-0/FIGURES/13.

[35] G. Liu, S. Zhang, J. Li, J. Wang, Q. Meng, Fast-heating for intercritical annealing of cold-rolled quenching and partitioning steel, Mater. Sci. Eng. A. 669 (2016) 387–395, https://doi.org/10.1016/J.MSEA.2016.05.106.

[36] X. Tan, W. Lu, X. Rao, Effect of ultra-fast heating on microstructure and mechanical properties of cold-rolled low-carbon low-alloy Q&P steels with different austenitizing temperature, Mater. Charact. 191 (2022) 112086, https://doi.org/10.1016/J.MATCHAR.2022.112086.

[37] T. Lolla, G. Cola, B. Narayanan, B. Alexandrov, S.S. Babu, Development of rapid heating and cooling (flash processing) process to produce advanced high strength steel microstructures, Mater. Sci. Technol. 27 (2011) 863–875, https://doi.org/10.1179/174328409X433813.

[38] V. Mattos Ferreira, M.G. Mecozzi, R.H. Petrov, J. Sietsma, Microstructure development of pearlitic railway steels subjected to fast heating, Mater. Des. 221 (2022) 110989, https://doi.org/10.1016/J.MATDES.2022.110989.

[39] S. Su, S. Quan, R. Song, Y. Wang, C. Cai, Microstructure-mechanical properties evolution of hot-rolled medium Mn steel: Effects of short-time holding and low-temperature tempering following ultrafast heating, Mater. Des. 238 (2024) 112658, https://doi.org/10.1016/J.MATDES.2024.112658.

[40] W. Mu, M. Rahaman, F.L. Rios, J. Odqvist, P. Hedström, Predicting strain-induced martensite in austenitic steels by combining physical modelling and machine learning, Mater. Des. 197 (2021) 109199, https://doi.org/10.1016/J.MATDES.2020.109199.

[41] S. Curtze, V.T. Kuokkala, A. Oikari, J. Talonen, H. Hänninen, Thermodynamic modeling of the stacking fault energy of austenitic steels, Acta Mater. 59 (2011) 1068–1076, https://doi.org/10.1016/J.ACTAMAT.2010.10.037.

[42] A. Dumay, J.P. Chateau, S. Allain, S. Migot, O. Bouaziz, Influence of addition elements on the stacking-fault energy and mechanical properties of an austenitic Fe–Mn–C steel, Mater. Sci. Eng. A. 483–484 (2008) 184–187, https://doi.org/10.1016/J.MSEA.2006.12.170.

[43] A. Saeed-Akbari, J. Imlau, U. Prahl, W. Bleck, Derivation and variation in composition-dependent stacking fault energy maps based on subregular solution model in high-manganese steels, Metall. Mater. Trans. A Phys. Metall. Mater. Sci. 40 (2009) 3076–3090, https://doi.org/10.1007/S11661-009-0050-8/TABLES/4.

[44] F. Zvavamwe, J. Pasco, G. Mishra, M.K. Paek, C. Aranas, Strengthening mechanisms in vanadium-microalloyed medium-Mn steels, Mater. Today Commun. 41 (2024) 110512, https://doi.org/10.1016/J.MTCOMM.2024.110512.

[45] J.K. Kim, B.C. De Cooman, Stacking fault energy and deformation mechanisms in Fe-xMn-0.6C-yAl TWIP steel, Mater. Sci. Eng. A. 676 (2016) 216–231, https://doi.org/10.1016/J.MSEA.2016.08.106.

[46] K. Jeong, J.E. Jin, Y.S. Jung, S. Kang, Y.K. Lee, The effects of Si on the mechanical twinning and strain hardening of Fe-18Mn-0.6C twinning-induced plasticity steel,

Acta Mater. 61 (2013) 3399–3410, https://doi.org/10.1016/j.actamat.2013.02.031.
[47] J.Y. Lee, Y.M. Koo, S. Lu, L. Vitos, S.K. Kwon, The behaviour of stacking fault energy upon interstitial alloying, Sci. Reports 71 (7) (2017) 1–6, https://doi.org/10.1038/s41598-017-11328-4.
[48] M. Zhao, L. Huang, C. Li, J. Li, P. Li, Evaluation of the deformation behaviors and hot workability of a high-strength low-alloy steel, Mater. Sci. Eng. A. 810 (2021) 141031, https://doi.org/10.1016/J.MSEA.2021.141031.
[49] N. Li, C. Zhao, Z. Jiang, H. Zhang, Flow behavior and processing maps of high-strength low-alloy steel during hot compression, Mater. Charact. 153 (2019) 224–233, https://doi.org/10.1016/J.MATCHAR.2019.05.009.
[50] M. Ali, A. Khosravifard, A. Hamada, T. Mattar, M. Eissa, J. Kömi, Promotion of thermomechanical processing of 2-GPa low-alloyed ultrahigh-strength steel and physically based modelling of the deformation behaviour, Mater. Sci. Eng. A. 867 (2023) 144747, https://doi.org/10.1016/J.MSEA.2023.144747.
[51] H.J. McQueen, N.D. Ryan, Constitutive analysis in hot working, Mater. Sci. Eng. A. 322 (2002) 43–63, https://doi.org/10.1016/S0921-5093(01)01117-0.
[52] F. Reyes-Calderón, I. Mejía, J.M. Cabrera, Hot deformation activation energy (QHW) of austenitic Fe–22Mn–1.5Al–1.5Si–0.4C TWIP steels microalloyed with Nb, V, and Ti, Mater. Sci. Eng. A. 562 (2013) 46–52, https://doi.org/10.1016/J.MSEA.2012.10.091.
[53] H. Moradjoo Hamedani, B. Tolaminejad, A. Momeni, S. Sadeghpour, Hot deformation behavior and microstructural characterization of a novel high entropy steel, Mater. Sci. Eng. A. 910 (2024) 146884, https://doi.org/10.1016/J.MSEA.2024.146884.
[54] A.S. Hamada, L.P. Karjalainen, M.C. Somani, The influence of aluminum on hot deformation behavior and tensile properties of high-Mn TWIP steels, Mater. Sci. Eng. A. 467 (2007) 114–124, https://doi.org/10.1016/J.MSEA.2007.02.074.
[55] M. Rout, S. Biswas, R. Ranjan, S.K. Pal, S.B. Singh, Deformation behavior and evolution of microstructure and texture during hot compression of AISI 304LN stainless steel, Metall. Mater. Trans. A Phys. Metall. Mater. Sci. 49 (2018) 864–880, https://doi.org/10.1007/S11661-017-4447-5/FIGURES/16.
[56] L. Li Chen, R. Luo, Y. Tong Yang, C.T. Peng, X. Gui, J. Zhang, K. Yang Song, P. Gao, X. Nong Cheng, Investigation on the hot deformation behavior of 316L stainless steel using 3D processing map, Trans. Indian Inst. Met. 72 (2019) 2997–3006, https://doi.org/10.1007/s12666-019-01674-4.
[57] A.S. Hamada, L.P. Karjalainen, M.C. Somani, R.M. Ramadan, Deformation mechanisms in high-al bearing high-Mn TWIP Steels in hot compression and in tension at low temperatures, Mater. Sci. Forum. 550 (2007) 217–222, https://doi.org/10.4028/0-87849-434-0.217.
[58] A. Rollett, G.S. Rohrer, J. Humphreys, Recrystallization and related annealing phenomena, Elsevier (2017), https://doi.org/10.1016/j.matchar.2020.110382.
[59] D. Ponge, G. Gottstein, Necklace formation during dynamic recrystallization: mechanisms and impact on flow behavior, Acta Mater. 46 (1998) 69–80, https://doi.org/10.1016/S1359-6454(97)00233-4.
[60] L. Zhao, N. Park, Y. Tian, A. Shibata, N. Tsuji, Combination of dynamic transformation and dynamic recrystallization for realizing ultrafine-grained steels with superior mechanical properties, Sci. Reports 61 (6) (2016) 1–11, https://doi.org/10.1038/srep39127.
[61] M. Jafari, A. Najafizadeh, Correlation between Zener–Hollomon parameter and necklace DRX during hot deformation of 316 stainless steel, Mater. Sci. Eng. A. 501 (2009) 16–25, https://doi.org/10.1016/J.MSEA.2008.09.073.
[62] K. Huang, R.E. Logé, A review of dynamic recrystallization phenomena in metallic materials, Mater. Des. 111 (2016) 548–574, https://doi.org/10.1016/J.MATDES.2016.09.012.
[63] A. Hamada, A. Khosravifard, D. Porter, L. Pentti Karjalainen, Physically based modeling and characterization of hot deformation behavior of twinning-induced plasticity steels bearing vanadium and niobium, Mater. Sci. Eng. A. 703 (2017) 85–96, https://doi.org/10.1016/J.MSEA.2017.07.038.
[64] A. Hamada, A. Khosravifard, S. Ghosh, M. Jaskari, A. Järvenpää, P. Karjalainen, High-speed erichsen testing of grain-refined 301LN austenitic stainless steel processed by double-reversion annealing, Metall. Mater. Trans. A Phys. Metall. Mater. Sci. 53 (2022) 2174–2194, https://doi.org/10.1007/S11661-022-06659-5/FIGURES/17.
[65] R.D. Doherty, Recrystallization and texture, Prog. Mater. Sci. 42 (1997) 39–58, https://doi.org/10.1016/S0079-6425(97)00007-8.
[66] S. Il Kim, Y.C. Yoo, Continuous dynamic recrystallization of AISI 430 ferritic stainless steel, Met. Mater. Int. 8 (2002) 7–13, https://doi.org/10.1007/bf03027023.
[67] F. Qin, H. Zhu, Z. Wang, X. Zhao, W. He, H. Chen, Dislocation and twinning mechanisms for dynamic recrystallization of as-cast Mn18Cr18N steel, Mater. Sci. Eng. A. 684 (2017) 634–644, https://doi.org/10.1016/J.MSEA.2016.12.095.
[68] A. Galiyev, R. Kaibyshev, G. Gottstein, Correlation of plastic deformation and dynamic recrystallization in magnesium alloy ZK60, Acta Mater. 49 (2001) 1199–1207, https://doi.org/10.1016/S1359-6454(01)00020-9.
[69] W.C. Cheng, C.K. Lai, Observing massive phase transformation in a Fe-Mn-Al alloy, Scr. Mater. 55 (2006) 783–786, https://doi.org/10.1016/j.scriptamat.2006.07.023.
[70] Y.V.R.K. Prasad, H.L. Gegel, S.M. Doraivelu, J.C. Malas, J.T. Morgan, K.A. Lark, D. R. Barker, Modeling of dynamic material behavior in hot deformation: Forging of Ti-6242, Metall. Trans. A. 15 (1984) 1883–1892, https://doi.org/10.1007/BF02664902/METRICS.
[71] H.Z. Paul Mansour Naghdi, Progress in Solid Mechanics, in: R.H. Ian NaismithSneddon, R. Hill (Eds.), Prog. Solid Mech., North-Holland Publishing Company, New York, 1963, pp. 93–193, https://doi.org/10.1115/1.3625865.
[72] S. Ghosh, A. Hamada, M. Patnamsetty, W. Borek, M. Gouda, A. Chiba, S. Ebied, Constitutive modeling and hot deformation processing map of a new biomaterial Ti–14Cr alloy, J. Mater. Res. Technol. 20 (2022) 4097–4113, https://doi.org/10.1016/J.JMRT.2022.08.160.
[73] Y.V.R.K. Prasad, K.P. Rao, S. Sasidhara, Hot Working Guide - A Compendium of Processing Maps, second, ASM International, 2015. https://www.asminternational.org/books-and-handbooks/results/-/journal_content/56/10192/25536184/PUBLICATION/ (accessed September 7, 2024).
[74] M. Patnamsetty, M.C. Somani, S. Ghosh, S. Ahmed, P. Peura, Processing map for controlling microstructure and unraveling various deformation mechanisms during hot working of CoCrFeMnNi high entropy alloy, Mater. Sci. Eng. A. 793 (2020) 139840, https://doi.org/10.1016/J.MSEA.2020.139840.
[75] A. Deshpande, P. Manda, C. Vanitha, A.K. Singh, Microstructural characterization of metastable beta titanium alloys in hot rolled and solution treated condition, Mater. Today Proc. 5 (2018) 3657–3663, https://doi.org/10.1016/J.MATPR.2017.11.616.
[76] M.C. Somani, E.S.B. Rao, N.C. Birla, M.L. Bhatia, V. Singh, Y.V.R.K. Prasad, Processing map for controlling microstructure in hot working of hot isostatically pressed powder metallurgy NIMONIC AP-1 superalloy, Metall. Trans. A. 23 (1992) 2849–2857, https://doi.org/10.1007/BF02651762/METRICS.
[77] C.M. Sellars, HOT WORKING (1986) 231–243, https://doi.org/10.1016/B978-0-08-033454-7.50019-X.
[78] J. Zhang, H. Di, Deformation heating and flow localization in Ti–15–3 metastable β titanium alloy subjected to high Z deformation, Mater. Sci. Eng. A. 676 (2016) 506–509, https://doi.org/10.1016/J.MSEA.2016.09.011.
[79] H. Rastegari, A. Kermanpur, A. Najafizadeh, D. Porter, M. Somani, Warm deformation processing maps for the plain eutectoid steels, J. Alloys Compd. 626 (2015) 136–144, https://doi.org/10.1016/J.JALLCOM.2014.11.170.
[80] Designation: E466 − 07 Standard Practice for conducting force controlled constant amplitude axial fatigue tests of metallic materials 1, (n.d.). https://doi.org/10.1520/E0466-07.
[81] C. Scott, B. Remy, J.L. Collet, A. Cael, C. Bao, F. Danoixd, B. Malardc, C. Curfse, Precipitation strengthening in high manganese austenitic TWIP steels, Int. J. Mater. Res. 102 (2011) 538–549, https://doi.org/10.3139/146.110508/MACHINEREADABLECITATION/RIS.
[82] C.P. Scott, F. Fazeli, B. Shalchi Amirkhiz, I. Pushkareva, S.Y.P. Allain, Structure-properties relationship of ultra-fine grained V-microalloyed dual phase steels, Mater. Sci. Eng. A. 703 (2017) 293–303, https://doi.org/10.1016/J.MSEA.2017.07.051.
[83] M. Schneider, J.P. Couzinié, A. Shalabi, F. Ibrahimkhel, A. Ferrari, F. Körmann, G. Laplanche, Effect of stacking fault energy on the thickness and density of annealing twins in recrystallized FCC medium and high-entropy alloys, Scr. Mater. 240 (2024) 115844, https://doi.org/10.1016/J.SCRIPTAMAT.2023.115844.
[84] D.P. Field, L.T. Bradford, M.M. Nowell, T.M. Lillo, The role of annealing twins during recrystallization of Cu, Acta Mater. 55 (2007) 4233–4241, https://doi.org/10.1016/J.ACTAMAT.2007.03.021.
[85] C. Song, Z. Zhang, W. Wu, H. Wang, Z. Cheng, Z. Sun, Y. Xia, W. Yin, H. Yu, Effect of Si on the deformation behavior of retained austenite and annealed martensite in medium Mn steels, Mater. Sci. Eng. A. 899 (2024) 146451, https://doi.org/10.1016/j.msea.2024.146451.
[86] A. Hamada, T. Juuti, A. Khosravifard, A. Kisko, P. Karjalainen, D. Porter, J. Kömi, Effect of silicon on the hot deformation behavior of microalloyed TWIP-type stainless steels, Mater. Des. 154 (2018) 117–129, https://doi.org/10.1016/J.MATDES.2018.05.029.
[87] T. Allam, M. Ali, X. Guo, S. Ghosh, C. Haase, M. Jaskari, A. Järvenpää, A. Hamada, Simultaneous enhancement of mechanical properties and resistance to hydrogen-assisted degradation by multiple precipitation and nano-twinning in medium manganese steel, Mater. Sci. Eng. A. 877 (2023) 145203, https://doi.org/10.1016/J.MSEA.2023.145203.
[88] K. Tsuzaki, Y. Natsume, Y. Tomota, T. Maki, Effect of solution hardening on the shape memory effect of FeMn based alloys, Scr. Metall. Mater. 33 (1995) 1087–1092, https://doi.org/10.1016/0956-716X(95)00337-U.
[89] A. Kisko, A.S. Hamada, J. Talonen, D. Porter, L.P. Karjalainen, Effects of reversion and recrystallization on microstructure and mechanical properties of Nb-alloyed low-Ni high-Mn austenitic stainless steels, Mater. Sci. Eng. A. 657 (2016) 359–370, https://doi.org/10.1016/J.MSEA.2016.01.093.
[90] R. Labusch, Statistische theorien der mischkristallhärtung, Acta Metall. 20 (1972) 917–927, https://doi.org/10.1016/0001-6160(72)90085-5.
[91] F.R.N. Nabarro, The theory of solution hardening, Philos. Mag. 35 (1977) 613–622, https://doi.org/10.1080/14786437708235994.
[92] M.Z. Butt, P. Feltham, Solid-solution hardening, J. Mater. Sci. 28 (1993) 2557–2576, https://doi.org/10.1007/BF00356192/METRICS.
[93] H. Sieurin, J. Zander, R. Sandström, Modelling solid solution hardening in stainless steels, Mater. Sci. Eng. A. 415 (2006) 66–71, https://doi.org/10.1016/J.MSEA.2005.09.031.
[94] L. Vegard, Die Konstitution der Mischkristalle und die Raumfüllung der Atome, Zeitschrift Für Phys. 5 (1921) 17–26, https://doi.org/10.1007/BF01349680/METRICS.
[95] G.E.D. Dieter, in: Bacon Mechanical Metallurgy, 3rd ed.,, McGraw-Hill, New York, 1976, https://doi.org/10.5962/bhl.title.35895.
[96] V. Javaheri, A. Pohjonen, J.I. Asperheim, D. Ivanov, D. Porter, Physically based modeling, characterization and design of an induction hardening process for a new slurry pipeline steel, Mater. Des. 182 (2019) 108047, https://doi.org/10.1016/J.MATDES.2019.108047.